JOURNAL OF GEOPHYSICAL RESEARCH, VOL. 112, B05307, doi:10.1029/2006JB004337, 2007

Click Here for Full Article

Correction published 18 November 2007

Aftershock asymmetry on a bimaterial interface

Allan M. Rubin[1] and Jean-Paul Ampuero[2]

Received 9 February 2006; revised 18 September 2006; accepted 31 January 2007; published 18 May 2007.

[1] To better understand the asymmetric distribution of microearthquake aftershocks along the central San Andreas fault, we study dynamic models of slip-weakening ruptures on an interface separating differing elastic half-spaces. Subshear ruptures grow as slightly asymmetric bilateral cracks, with larger propagation velocities, slip velocities, and normal stress changes at the rupture front moving in the direction of slip of the medium with the lower shear wave speed (the southeast front, in the context of the San Andreas). When the SE front encounters a stress barrier, the tensile stress perturbation behind the rupture front continues forward and for a wide range of barrier strengths nucleates a dying slip pulse. This slip pulse smooths the stress field and reduces the static stress change beyond the SE front. Furthermore, because the tensile stress that carried the slip pulse into the barrier is a purely dynamic phenomenon, the SE rupture front can be left far below the failure threshold, while the NW front remains quite close to failure. Both mechanisms could contribute to the observed aftershock asymmetry. Formation of a robust slip pulse requires a peak tensile stress perturbation that approaches the nominal strength drop of the slip-weakening law. To achieve this while minimizing off-fault damage requires either substantial velocity contrasts or small reductions in friction. The simulations also show a pronounced asymmetry in the timescales over which barriers to the SE and NW experience increasing stresses, a result that has implications for the asymmetric distribution of subevents in compound earthquakes.

Citation: Rubin, A. M., and J.-P. Ampuero (2007), Aftershock asymmetry on a bimaterial interface, *J. Geophys. Res.*, *112*, B05307, doi:10.1029/2006JB004337.

1. Introduction

[2] Large crustal faults are likely to juxtapose rocks with different mechanical properties, with important implications for earthquake behavior. From symmetry, slip along a planar fault in a homogeneous linear elastic body induces no change in normal stress on the fault. For in-plane or Mode-II slip along a fault separating differing elastic materials, this symmetry is lost. Near the tips of dynamically propagating ruptures the normal stress changes that result can be quite large. This in turn influences the slip.

[3] *Weertman* [1980] derived analytic solutions for the steady-state propagation of a pulse along a bimaterial interface at less than the slower shear wave speed. Conceptually, the fault operated under a constant coefficient of friction f and was subjected to a uniform ambient shear stress τ^{∞} and normal stress σ_n^{∞} such that $\tau^{\infty}/\sigma_n^{\infty} < f$. Under these conditions a steady-state pulse is feasible only because of the coupling between shear slip and normal stress. Changes in normal stress occur only where the slip gradient is nonzero, so ahead of the pulse the change in normal stress is zero. In the actively slipping region behind the pulse front, the normal stress change is tensile for pulses propagating in the direction of slip of the more compliant material (defined more precisely below), and compressive for pulses moving in the opposite direction. Thus Weertman deduced that for these boundary conditions pulses might run only in the direction of slip of the more compliant medium (hereafter termed the "positive" direction). *Adams* [1998] subsequently found a steady solution in the form of a wave train with piecewise-constant slip velocities (alternately zero and nonzero), with either constant or velocity-dependent friction.

[4] Most early numerical studies examined the case of a constant coefficient of friction and an ambient shear stress that lies below the failure threshold [*Andrews and Ben-Zion*, 1997; *Ben-Zion and Andrews*, 1998; *Cochard and Rice*, 2000]. Rupture was initiated by a localized (both spatially and temporally) region of elevated pore pressure. Typically, self-healing pulses were generated; these moved in the positive direction at velocities slightly below the slower shear wave speed. For some initial conditions, *Cochard and Rice* [2000] obtained pulses that moved in the opposite ("negative") direction at about the slower of the two compressional wave speeds. Supershear rupture fronts moving in the negative direction were also observed experimentally by *Xia et al.* [2005], when the ambient load was moderately close to failure. Whether rupture was crack-like or pulse-like in these experiments was difficult to determine,

[1]Department of Geosciences, Princeton University, Princeton, New Jersey, USA.
[2]Institute of Geophysics, Swiss Federal Institute of Technology, Zurich, Switzerland.

Copyright 2007 by the American Geophysical Union.
0148-0227/07/2006JB004337$09.00

but it was bilateral. Rupture was initiated using an explosive wire, which qualitatively resembles the nucleation procedure in the above numerical simulations. *Harris and Day* [1997], on the other hand, used a slip-weakening model (lower dynamic than static friction) with loading stresses that did not decrease so abruptly and produced crack-like growth. For subshear ruptures the propagation velocities of the two fronts were nearly identical; asymmetry was most apparent in that slip velocities near the front moving in the positive direction were much larger than those at the opposite front. Cochard and Rice suggested that this crack-like behavior resulted from the different initiation procedures as well as the different constitutive laws. Indeed, *Shi and Ben-Zion* [2006] obtained mostly unidirectional pulses using a slip-weakening law in which rupture was again initiated with a spatially and temporally localized elevated pore pressure. However, the excess pressure returned to its ambient value before the slip-weakening distance was reached and, except for their lowest dynamic friction values, before the fault strength dropped below the ambient shear stress. Under such conditions it is not surprising that their simulations were dominated by slip pulses propagating in the positive direction.

[5] Despite the obvious asymmetry in these numerical simulations, geological evidence of a bimaterial effect in earthquake rupture has been difficult to come by. *Harris and Day* [2005] point out that of the eight magnitude 4–6 earthquakes occurring on the San Andreas fault near Parkfield, California since 1934, five propagated to the northwest (NW), while only three propagated to the southeast (SE). At seismogenic depths this region has lower-velocity rocks to the northeast, so the expected direction of preferred propagation for subshear ruptures is to the SE. *Ben-Zion* [2006] counters that this apparent discrepancy might be due to a combination of (1) the statistics of small numbers, (2) a structurally complex fault zone, with two major slip surfaces having velocity contrasts of the opposite sense, and (3) the possibility that ruptures might have to extend vertically throughout the entire seismogenic zone, so as to become strictly mode-II ruptures, for bimaterial effects to dominate (but see *Harris and Day* [2006] for a reply). Recently, *Dor et al.* [2005, 2006] reported that near-surface damage occurs predominantly on one side of major strike-slip faults in California and Turkey. They propose that this results from unidirectional ruptures that consistently propagate in the positive direction, with damage being concentrated on the tensile (higher-modulus) side of the rupture front. Seismic velocity models are not available for all of these sites, but those that exist are consistent with this interpretation.

[6] Evidence suggestive of a bimaterial effect was also described by *Rubin and Gillard* [2000] and *Rubin* [2002a]. They used waveform cross-correlation to obtain precise relative locations for nearly 5000 magnitude 1–3 earthquakes distributed over 60 km of the San Andreas fault near San Juan Bautista. As at Parkfield, lower velocity rocks here lie to the NE [*Eberhart-Phillips and Michael*, 1998; *Rubin*, 2002a; *McGuire and Ben-Zion*, 2005], so the expected direction of preferred propagation for subshear ruptures is to the SE. Roughly 300 of the microearthquakes had aftershocks that occurred within 10 hours and roughly 2 mainshock radii of the mainshock centroid. Of the 169 aftershocks beyond the mode-II edges of the mainshock, 125 occurred to the NW and 44 to the SE. In a coin toss such lopsided results have a probability of occurrence of 10^{-9}. In contrast, beyond the mode-III ends of the mainshock, where bimaterial effects are expected to be unimportant, 61 aftershocks were shallower and 64 deeper. In addition, no asymmetry was observed along the Calaveras fault, where no velocity contrast was observed [*Rubin*, 2002a]. Along the San Andreas fault, significant asymmetry was absent at distances larger than $\sim$2 mainshock radii and for time delays longer than $\sim$1 day (Figure 1). While the aftershock density to the NW peaks in the distance range of 1–2 radii, as would be expected from a simple stress transfer model, the peak density to the SE lies in the 2–3 radii range. The simplest interpretation is that this reflects a deficit of the nearest aftershocks to the SE.

[7] *Rubin and Gillard* [2000] proposed that because of the extra dynamic "kick" (tensile stress) associated with the SE-propagating rupture front, barriers that stopped that front would be stronger, in a statistical sense, than those that stopped the NW-propagating front. Once the rupture stops, the quasi-static stress change is much more symmetric, causing the region to the SE to remain farther from failure and making short-term aftershocks to the NW more likely. To this possibility *Rubin* [2002a] added the following: For a nucleation zone to produce an aftershock within 10 hours, it presumably should have been close to failure at the time of the mainshock. Because of the large tensile stress accompanying dynamic propagation of the SE rupture front, any such nucleation zone lying to the SE might instead have become part of the mainshock. The key point underlying both explanations is that this dynamic tensile stress is both transient and asymmetric. The purpose of this paper is to explore these explanations more quantitatively.

[8] We begin with an overview of the bimaterial problem, emphasizing Weertman's analytical results and our scheme for regularizing the response of the fault surface to normal stress changes. In section 3.1 we consider growing cracks, concentrating on the normal stress changes and resulting behavior near the SE rupture front. We then use Weertman's results to make dimensional estimates of the changes in both the fault-normal and fault-parallel stresses near the SE rupture front and find these estimates to be sufficiently accurate to be of use in thinking one's way through parameter space. Section 3.3 presents the main results of this paper, the behavior of ruptures as they are slowed and stopped by symmetric stress barriers, and the role of the slip pulse spawned by the dying SE rupture front in generating asymmetries in the dynamic and residual stress fields. We briefly look at loading conditions that lead to supershear rupture velocities to the NW, and again consider the magnitudes of the off-fault stresses. Finally, in section 4 we use a simplified rate-and-state friction formulation to make a crude estimate of the aftershock asymmetry that might result from our computed quasi-static and dynamic stress distributions, and briefly discuss other processes (e.g., rate-and-state behavior; thermal weakening) that might influence aftershock asymmetry on natural faults. We also consider observations of asymmetry in off-fault damage and in the distribution of

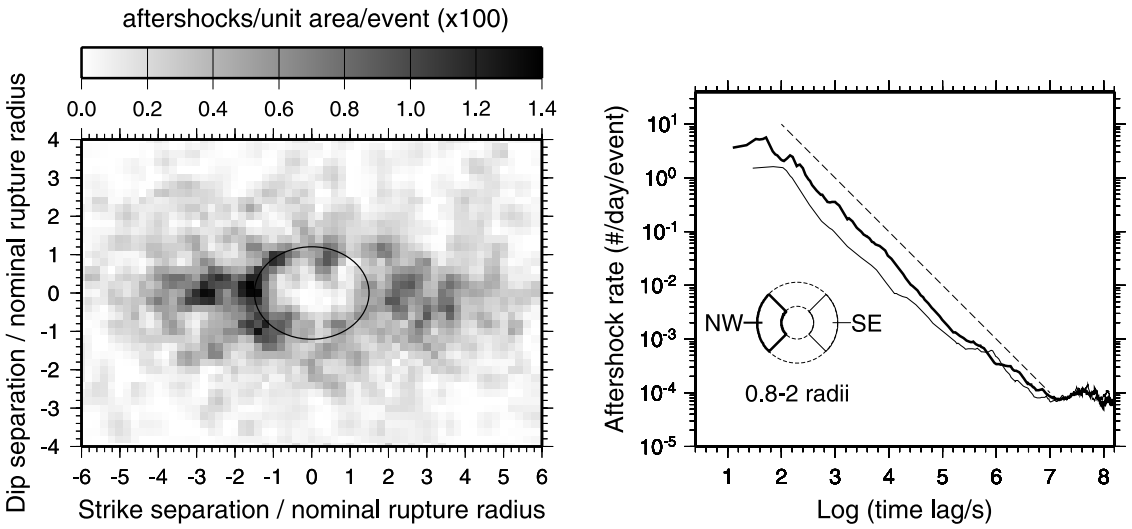

Figure 1. (left) Stacked aftershock sequences of 5000 microearthquakes along 60 km of the San Andreas fault near San Juan Bautista, from *Rubin* [2002a]. Distances are normalized by the mainshock radius, estimated assuming circular ruptures with a 10-MPa stress drop and the moment-magnitude relation of *Abercrombie* [1996]. The ellipse, symmetric about the origin, corresponds to a stress drop of 4.5 MPa. Asymmetry is restricted to $\sim$1–2 mainshock radii. (right) Seismicity rate as a function of time following the composite mainshock, for aftershocks from 0.8 to 2 estimated radii to the NW (thick line) and SE (thin line), showing the factor of $\sim$3 difference at early times and the near symmetry for time delays greater than a few days (1 day $\sim 10^5$ s). The dashed line shows a decay of 1/time.

subevents in compound earthquakes in light of our numerical results.

2. Problem Formulation

2.1. Model Geometry

[9] We consider the two-dimensional (2-D) system illustrated in Figure 2. The fault lies on the boundary between an upper, more compliant medium, with shear modulus μ_1, Poisson's ratio ν_1, and density ρ_1, and a lower, stiffer medium with corresponding properties μ_2, ν_2, and ρ_2. The elastic shear and compressional wave speeds are C_{S_1} and C_{P_1} for the upper half space and C_{S_2} and C_{P_2} for the lower. The fault motion is in-plane and right-lateral, so in the context of the San Andreas fault the positive (right) and negative (left) directions correspond respectively to SE and NW, as indicated.

2.2. Bimaterial Background

[10] The dynamic properties of the medium are determined by the four dimensionless parameters μ_2/μ_1, ρ_2/ρ_1, ν_2, and ν_1. In light of the analytical results of *Weertman* [1980], we argue below that the most important parameter is the ratio C_{S_2}/C_{S_1}. We find that a key measure of asymmetry is the magnitude of the tensile stress perturbation associated with the SE-propagating rupture front. Weertman showed that for steady-state propagation of a slip pulse the shear and normal stress changes along the fault plane are given by

$$\Delta\tau(x) = \frac{\bar{\mu}}{2\pi}\int_{-\infty}^{\infty}\frac{\mathrm{d}\delta/\mathrm{d}s}{x-s}\mathrm{d}s, \tag{1}$$

$$\Delta\sigma_n(x) = \mu^*\frac{d\delta}{dx}, \tag{2}$$

where δ is slip. The moduli $\bar{\mu}$ and μ^* are functions of both the elastic properties and the rupture velocity, and are given in Appendix A. To simplify later expressions, we have defined $\bar{\mu}$ to be twice Weertman's value. Note that the shear stresses are sensitive to slip gradients all along the fault but that the normal stresses depend only upon the local gradient. For a homogeneous medium $\mu^* = 0$ and $\bar{\mu}_0 = \mu/(1-\nu)$, where μ is the shear modulus, ν is Poisson's ratio, and the subscript 0 denotes quasi-static deformations. The latter relation and equation (1) motivate us to define the effective shear modulus μ' of a bimaterial to equal $\bar{\mu}_0$.

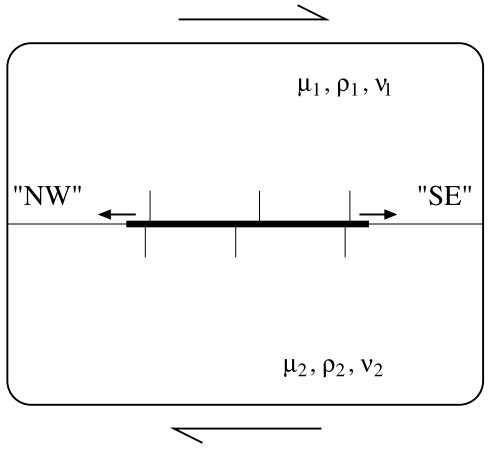

Figure 2. Model geometry. A right-lateral rupture (thick line) runs along the interface between half-spaces with the indicated properties. For $\mu_2/\rho_2 > \mu_1/\rho_1$ the preferred propagation direction for subshear ruptures (the positive direction) is to the right. In the context of the San Andreas fault this corresponds to SE.

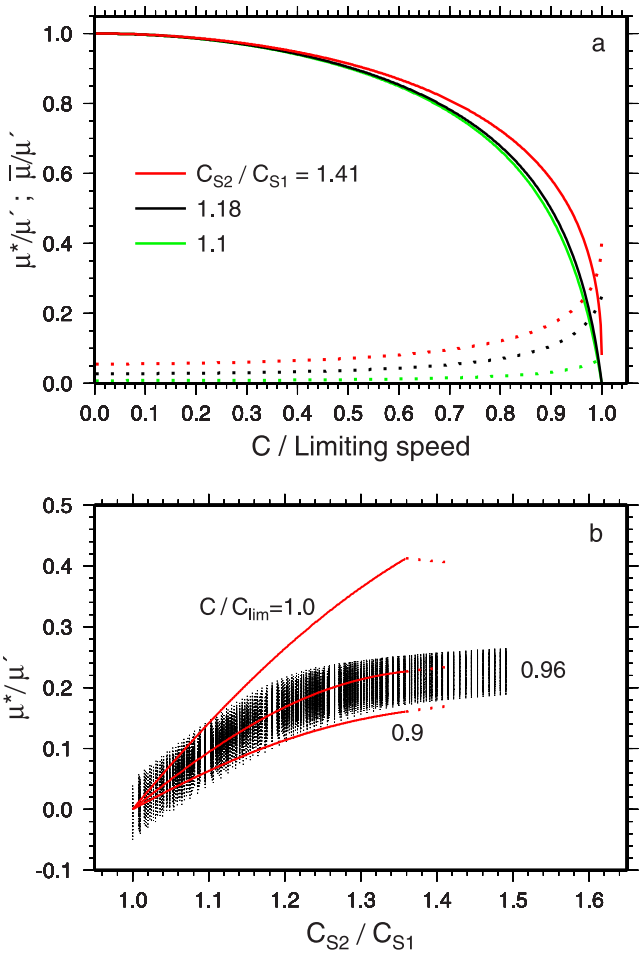

Figure 3. (a) Plots of μ^* (dotted lines) and $\bar{\mu}$ (solid), normalized by the effective static elastic modulus of the bimaterial μ', as a function of the normalized rupture speed C/C_{lim} for C_{S_2}/C_{S_1} = 1.1 (green lines), 1.18 (black), and 1.41 (red). In each case $\rho_2/\rho_1 = 1.0$ and $\nu_2 = \nu_1 = 0.25$. For $C_{S_2}/C_{S_1} = 1.41$, $\bar{\mu}$ does not decrease to zero by $C/C_{S_1} = 1$ so C_{GR} does not exist and $C_{lim} = C_{S_1}$. (b) μ^*/μ' as a function of C_{S_2}/C_{S_1}, at velocities of 90%, 96%, and 100% of the limiting speed. Lines show the case $\rho_2/\rho_1 = 1.0$ and $\nu_2 = \nu_1 = 0.25$, and are dotted where C_{GR} does not exist. Dots show the results of a grid search at $C/C_{lim} = 0.96$, with $1 \le \mu_2/\mu_1 \le 2$, $0.2 \le \nu_2 \le 0.34$, $0.2 \le \nu_1 \le 0.38$, and $0.9 \le \rho_2/\rho_1 \le 1.3$.

[11] The modulus $\bar{\mu}$ decreases with increasing propagation velocity, and for small to moderately large material contrasts there is a velocity at which it (and hence $\Delta\tau$) is zero (Figure 3a). By analogy with the Rayleigh wave speed in a homogeneous body, this velocity is referred to as the generalized Rayleigh speed C_{GR}. When it exists, C_{GR} lies between the Rayleigh speeds of the two media and is slower than C_{S_1}, and serves as a speed limit for subshear ruptures. When C_{GR} does not exist, we find numerically that C_{S_1} acts as a speed limit. The modulus μ^* is typically only a few percent of μ' at low propagation velocities but can become much larger near the limiting speed (Figure 3a).

[12] Under quasi-static conditions the sign of μ^* can be intuited from the following: In a homogeneous medium, slip on a planar fault loaded as in Figure 2 indices a counterclockwise rotation. From symmetry, the normal stress changes along the fault and its planar extension are zero [*Andrews and Ben-Zion*, 1997]. If one then imagines that the fault separates two half-spaces, one of which (say the lower) is rigid, the same slip produces no rotations (we assume the confining pressure to be large enough to prevent the fault surfaces from separating). The normal stress change in the latter case can be estimated by considering what normal stresses must be applied to the surface of the upper half space, in the homogeneous case, to bring the normal displacements back to zero. Clearly, the required stresses are tensile near the end of the fault that moves upward (the end on the right), and compressive at the opposite end. In other words, the stress change is tensile at the end of the fault that lies in the direction of slip of the more compliant medium. From equation (A7) in Appendix A, "compliance" in this case is $(1-2\nu)/\mu$, as might be expected since fault rotation in a homogeneous body is proportional to this quantity [*Pollard and Segall*, 1987].

[13] It is difficult to discern by inspection what determines the sign and magnitude of μ^* at dynamic speeds. We find via a grid search ($1 \le \mu_2/\mu_1 \le 2$; $0.2 \le \nu_2 \le 0.34$; $0.2 \le \nu_1 \le 0.38$; $0.9 \le \rho_2/\rho_1 \le 1.3$) that by far the most diagnostic simple elastic parameter is C_{S_2}/C_{S_1}. The dots in Figure 3b show the normalized values of μ^* at a propagation velocity equal to 96% of the limiting speed. The red lines are for $\nu_1 = \nu_2 = 0.25$ and $\rho_2/\rho_1 = 1$, at velocities of 90% (bottom), 96%, and 100% (top) of the limiting speed. Under these conditions C_{GR} exists for $C_{S_2}/C_{S_1} \lesssim 1.359$ [*Harris and Day*, 1997]. That the sign of μ^* is controlled by the ratios of $(1-2\nu)/\mu$ at low speeds but (predominantly) C_S at large speeds means that μ^* may change sign with increasing velocity. However, below this transition the magnitudes of both μ^* and typical displacement gradients, and hence any normal stress changes, are small.

2.3. Constitutive Law

[14] Although a constant coefficient of friction is capable of producing an elastic instability through normal stress changes alone, there is no evidence that this is the case for the earthquakes we seek to explain. Most of these come from the creeping section of the San Andreas fault, which presumably is creeping because the bulk of the fault is steady-state velocity strengthening in the sense of rate-and-state friction. The microearthquakes themselves represent small patches of the fault that are capable of instability, so clearly something distinguishes them from their surroundings. Because of the material contrast, it may be possible (at least in 2-D, as shown by *Rice et al.* [2001]) that the microearthquakes represent slightly velocity-strengthening regions in a strongly velocity-strengthening background, but we neglect this possibility here.

[15] For simplicity we adopt a slip-weakening friction law with the shear stress given by

$$\tau(x) \le f(-\sigma_n^* - p) \,, \tag{3}$$

where the equality holds where the fault is slipping and the inequality where it is locked and where σ_n^* (negative in

compression) is an effective normal stress defined below. As in most previous bimaterial studies we assume the pore pressure p to be independent of slip, although it undoubtedly is not, and omit it from subsequent expressions. The coefficient of friction f varies linearly with slip from a peak or static value f_s to a residual or dynamic value f_d over a critical slip distance δ_c:

$$f = f_s - (f_s - f_d)\frac{\delta}{\delta_c}\ ,\ 0 \le \delta \le \delta_c\ ; \tag{4}$$

$$f = f_d\ ,\ \delta > \delta_c\ . \tag{5}$$

[16] Unless stated otherwise, we fix $f_s = 0.7$, $f_d = 0.6$, and $\delta_c = 6$ mm. In the following, we write $\Delta\tau^{p-r}$ for the nominal peak-to-residual strength drop in the absence of normal stress changes; that is, $\Delta\tau^{p-r} \equiv -\sigma_n^{\infty}\Delta f$, where $\Delta f \equiv f_s - f_d$.

[17] *Ranjith and Rice* [2001] and *Cochard and Rice* [2000] emphasize that when C_{GR} exists (and for likely values of f even when it does not), formulations in which the frictional strength responds instantaneously to changes in σ_n are ill-posed in that (1) perturbations to steady sliding of all wavelengths are unstable and (2) the growth rate of the instability is inversely proportional to wavelength. This implies that numerical simulations do not converge with grid refinement. Regularization of such problems can be achieved by giving the frictional strength a fading memory of past normal stresses, in much the same way that the "state variable" in rate-and-state friction evolves continuously with slip or time. If normal stress affects frictional strength by altering the true contact area of the surfaces, then a minimum timescale for the evolution of contact area might be that required for the gaps between asperities to communicate their size to those asperities (that is, treating those gaps as cracks with stress concentrations at their tips). If the asperity size is D and the true contact area is 1% of the nominal contact area, then a typical asperity spacing is $10D$ and an estimate of this time is $10D/C_S$. For $C_S = 3$ km/s and $D = 10$ μm, this time is 10^{-1}–10^{-2} μs. Chemical bonding between the surfaces might increase this time scale.

[18] Experimental studies have established the existence of a fading memory of past normal stresses but not its nature. In GPa-scale shock wave experiments with slip speeds of tens of meters per second, *Prakash* [1998] observed that a step decrease in normal stress resulted in a continuous reduction in shear stress over a timescale of order 10^{-1} μs or a slip scale of order 1 μm. In a more classical rock friction geometry with normal stresses of order 5 MPa and slip speeds of 1 μm/s, *Linker and Dieterich* [1992] observed an "instantaneous" drop in frictional strength for an abrupt drop in normal stress, followed by an approach to steady-state over a timescale of order 1 s or slip scale (again) of order 1 μm. The experiments of Linker and Dieterich lacked a high-speed recording system with which to resolve short-duration transients, and in fact their "abrupt" changes in normal stress had estimated rise times of order 0.1 s. However, even if we assume that a short-duration transient was present, their experiments still differ from those of *Prakash* [1998] in that most of the strength drop occurred over a very short slip scale, with the resolvable strength drop over a slip scale of 1 μm producing only a modest fraction of the total.

[19] By analogy with *Cochard and Rice* [2000], we can regularize the governing equations by forcing the "effective" normal stress σ_n^* that multiplies the friction coefficient in equation (3) to vary continuously according to

$$\dot{\sigma}_n^* = \frac{\alpha|v| + v^*}{\delta_\sigma}(\sigma_n - \sigma_n^*)\ . \tag{6}$$

[20] Here v is the local slip speed, α takes on the value 0 or 1, σ_n is the normal stress, and v^* and δ_σ are a reference slip speed and distance. By "effective," we mean not the common definition of normal stress minus the pore pressure but the normal stress relevant to the surface strength; that is, the normal stress that at steady-state would give rise to the current contact area. For $\alpha = 0$ σ_n^* evolves with time, and for $v^* = 0$ it evolves with slip.

[21] We think it reasonable that at slow (or zero) slip speeds the strength of the surface will vary with time in response to a changing normal stress, but that at high slip speeds the strength may vary with slip as well. Existing experiments do not distinguish between time- and slip-dependence. The key issue here is whether σ_n^* tracks σ_n closely on the length scale of the slip-weakening region near the rupture front, where the displacement gradients and hence normal stress changes are large. Large asymmetries arise most readily if σ_n^* evolves rapidly on this scale, and we assume this to be the case. Such an interpretation does not find much support from the experiments of *Prakash* [1998], where the slip scale for stress evolution ($\sim$1 μm) was close to that observed for the evolution of shear stress in constant-normal-stress velocity-stepping experiments (it is the latter sort of experiment that a slip-weakening model is intended to mimic). However, rapid evolution does appear to be consistent with the rock friction experiments of *Linker and Dieterich* [1992], where most of the strength reduction occurred over a much shorter slip scale than that observed in velocity-stepping experiments (also $\sim$1 μm).

[22] We find that for the distances our subshear ruptures propagate, the precise values of α and v^* in (6) matter little provided the evolution of σ_n^* near the rupture front is rapid compared to the evolution of f (one exception is noted in section 3.1). Setting $\alpha = 0$ (pure time dependence) has the advantage of enabling one to guarantee beforehand that a particular simulation is well-resolved numerically, however large the slip velocity becomes. This results in somewhat noisy stopping phases, however. Therefore we typically enforce rapid evolution of σ_n^* by choosing $\alpha = 1$, v^* to be a characteristic near-tip slip speed (4 m/s), and $\delta_\sigma \ll \delta_c$ (typically $\delta_\sigma/\delta_c = 0.2$).

2.4. Initial Conditions and Numerical Method

[23] In all cases we impose a uniform ambient normal stress $\sigma_n^{\infty} = -100$ MPa. With $f_s = 0.7$ and $f_d = 0.6$ this yields peak and residual shear stresses (in the absence of normal stress changes) of 70 and 60 MPa. The ambient shear stress is

$$\tau^{\infty} = \tau_{bg} + \Delta\tau_{barr} + \Delta\tau_{nuc} + \Delta\tau_{init}\ , \tag{7}$$

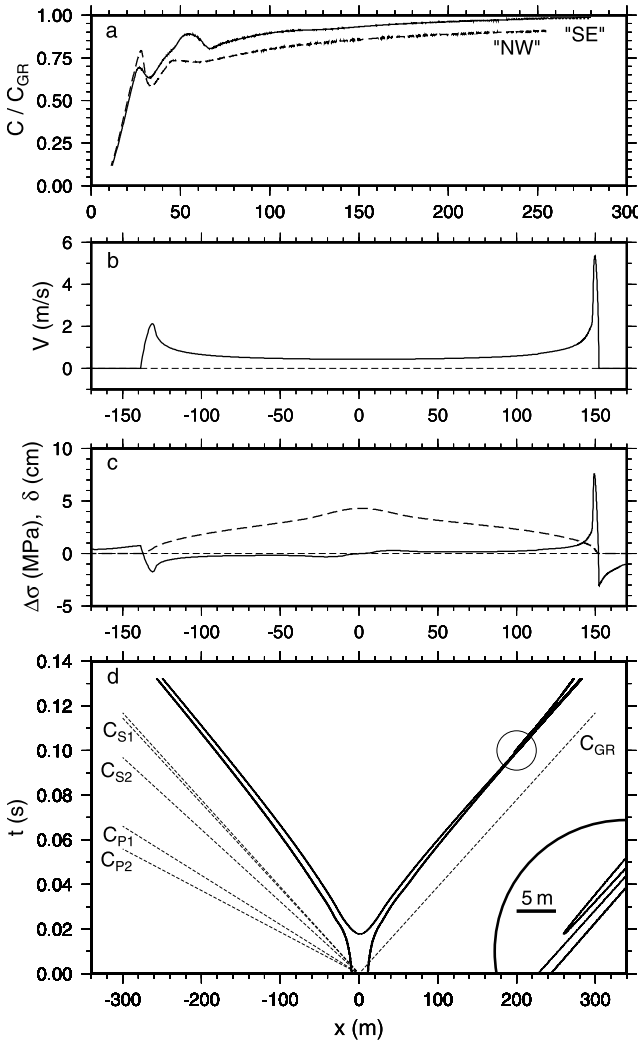

Figure 4. Results for $C_{S_2}/C_{S_1} = 1.18$, $v_2 = v_1 = 0.25$, and $\rho_2/\rho_1 = 1$, with $C_{S_1} = 2620$ m/s, $\sigma^\infty = -100$ MPa, $f_s = 0.7$, $f_d = 0.6$, $\delta_c = 6$ mm, $\Delta x = 6.25$ cm, and (in equation (6)) $\alpha = 0$, $v^* = 4$ m/s, and $\delta_\sigma/\delta_c = 0.1$. $C_{GR} = 2571$ m/s. (a) The propagation velocity at the "NW" (dashed) and "SE" (solid) rupture fronts, smoothed over a propagation distance of 2 m. The two curves bracket the rate of approach to C_{GR} obtained numerically for the same loading and slip-weakening parameters in a homogeneous medium, and also the rate estimated analytically using the results of *Freund* [1990] for self-similar crack growth and the constraint $G = G_c$. (b) The slip velocity and (c) the normal stress change $\Delta\sigma_n$ (solid) and slip δ (dashed) when the rupture is about 300 m across. (d) Space-time plot showing the rupture front (outer solid lines) and tail end of the slip-weakening region (inner solid lines). Inset enlarges the onset of the pulse spawned by the SE front; wedge-shaped region is the zero-slip-speed contour. Dashed lines show the indicated wave speeds.

where τ_{bg} is a uniform background value larger than $|\sigma_n^\infty| f_d$, $\Delta\tau_{barr}$ is a shear stress barrier placed at some distance from the origin to stop the rupture, and $\Delta\tau_{nuc}$ is a locally elevated shear stress that serves to localize nucleation. The latter is given by

$$\Delta\tau_{nuc} = A_{nuc}[\cos(\pi x/L_{nuc}) + 1] \ , \ |x| \le L_{nuc} \ , \qquad (8)$$

with $A_{nuc} \sim 4$ MPa and $L_{nuc} \sim 30$ m. Superimposed on a slowly increasing τ_{bg}, this gives rise to elastic instability before the maximum slip reaches δ_c. To the extent that bimaterial effects are small at low slip speeds, the nucleation results of *Uenishi and Rice* [2003] for homogeneous media then apply. They find a "universal" nucleation half-length equal to $0.579\mu'/W$, where W is the slip weakening rate $|\sigma_n^\infty|\Delta f/\delta_c$. We explore various moduli contrasts but maintain $\mu' = 29.25$ GPa and $v_2 = v_1 = 0.25$, for which the Uenishi and Rice nucleation half-length is 10.1 m.

[24] We nucleate in a static elastic boundary element code [*Crouch and Starfield*, 1983] using an element length of 12.5 cm. Starting near instability, we increase τ_{bg} in small increments until a stable configuration can no longer be found. For the above values of μ', W, A_{nuc}, and L_{nuc}, this last stable τ_{bg} is ~62.83 MPa, which for homogeneous media is low enough to ensure subshear rupture speeds (this requires $[\tau_{bg} - \tau_d]/\Delta\tau^{p-r} < 0.36$ [*Andrews*, 1985], where τ_d is the residual shear stress $|\sigma_n^\infty| f_d$; in this example $[\tau_{bg} - \tau_d]/\Delta\tau^{p-r} = 0.28$). We also run a limited number of cases with $f_d = 0.55$ (and and a larger δ_c to maintain the same W), which quickly leads to supershear speeds at the NW rupture front ($[\tau_{bg} - \tau_d]/\Delta\tau^{p-r} = 0.52$). For moduli contrasts up to $\mu_2/\mu_1 = 2$ we find that the nucleation zone is only 2% longer than the Uenishi and Rice estimate and offset in the positive direction by <1 m.

[25] For the elastodynamic calculation we use the spectral boundary integral code developed by *Cochard and Rice* [2000]. The initial displacements and (perturbed) normal and shear stresses are provided by the output of the quasi-static code, with the shear stress increased uniformly by $\Delta\tau_{init}$ (0.01 or 0.1 MPa) to initiate motion (we have found the difference between these two values to be irrelevant for our purposes). The fault of length L_x is discretized into n_x gridpoints with spacing Δx. The spectral approach results in replicates of the growing rupture spaced every L_x, which we take to be large enough that they do not interfere with one another. As suggested by *Breitenfeld and Geubelle* [1998], the timestep is taken to be $0.4(\Delta x/C_{S_2})$. Memory limitations restrict most runs to be carried out with $n_x = 2^{14}$ on 16 processors; with $L_x = 1024$–2048 m this results in $\Delta x = 6.25$–12.5 cm. This is more than sufficient to resolve the slip-weakening region near the rupture front. A more stringent requirement is to resolve the evolution of σ_n^*. For $v \gg v^*$, as may happen very near the limiting speed, the ratio of the slip scale for the evolution of σ_n^* to that for the evolution of f is δ_σ/δ_c. For $\delta_\sigma/\delta_c = 0.2$ and a 2-m slip pulse or slip-weakening zone, resolving σ_n^* requires $\Delta x \ll 40$ cm.

3. Results

[26] Unless otherwise noted, the simulations shown below are run with $\sigma_n^\infty = -100$ MPa, $f_s = 0.7$, $f_d = 0.6$, $\tau_{bg} = 62.83$ MPa, $\delta_c = 6$ mm, $\delta_\sigma/\delta_c = 0.2$, $\alpha = 1$, $v^* = 4$ m/s, $v_1 = v_2 = 0.25$, and $\rho_2/\rho_1 = 1$. We consider three ratios of μ_2/μ_1 (1.2, 1.4, and 2.0) while maintaining $\mu' = 29.25$ GPa. With $C_S = (\mu/\rho)^{1/2}$ this yields ratios C_{S_2}/C_{S_1} of 1.10, 1.18, and 1.41; in the latter case C_{GR} does not exist.

3.1. Growing Ruptures

[27] Results of a simulation with $C_{S_2}/C_{S_1} = 1.18$ are shown in Figure 4. With no barriers we use $\alpha = 0$ (time

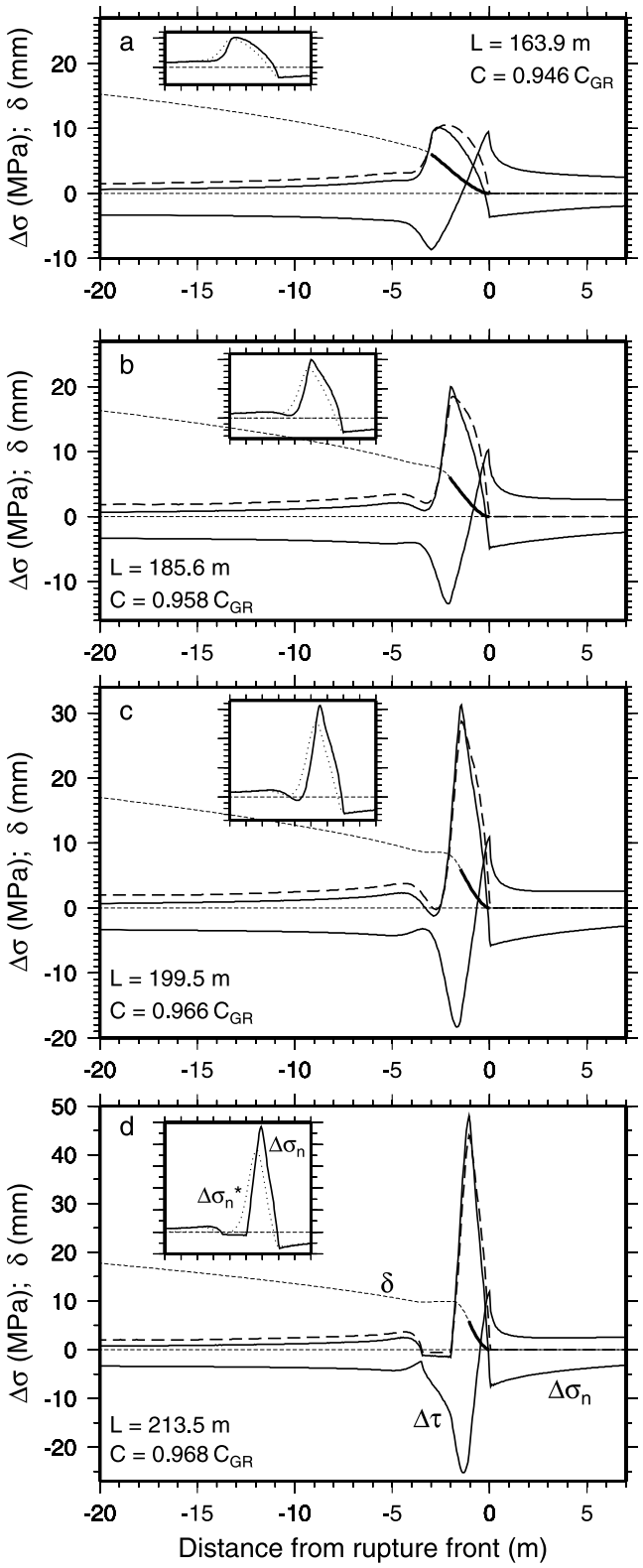

Figure 5. Four snapshots of $\Delta\sigma_n$ and $\Delta\tau$ (solid lines) and δ (thin dashed lines; bold segments show the slip-weakening region) at the SE rupture front for the simulation of Figure 4. The thick dashed lines indicate the steady-state estimate of $\Delta\sigma_n$ from equation (2). The rupture front position L and speed C are indicated. Insets compare $\Delta\sigma_n$ to the "effective" normal stress change $\Delta\sigma_n^*$ from equation (6).

evolution of σ_n^*) with $\delta_\sigma/\delta_c = 0.1$ and $v^* = 4$ m/s, so that the tip region remains well-resolved even in the face of the large slip velocities that ensue. Growth is crack-like rather than pulse-like, as expected for our adopted loading conditions, but asymmetry is manifested in several ways. The SE rupture front approaches the limiting speed (C_{GR}) more rapidly than does the NW front (Figure 4a). This disparity is considerably larger than is seen in the simulations of *Harris and Day* [1997], perhaps because they have poor resolution within the slip-weakening region. As in the simulations of Harris and Day, slip velocities are much larger at the SE front (Figure 4b). The normal stress changes at the two fronts are antisymmetric but are again consistently larger to the SE (Figure 4c).

[28] The space-time plot in Figure 4d indicates the location of the rupture fronts (outer solid lines) and the tail of the slip-weakening region ($\delta = \delta_c$; inner solid lines). Slip near the origin reaches δ_c by about 0.02 s, at which point (coincidentally) the rupture fronts accelerate rapidly. The slip-weakening zone behind the SE-propagating front shortens continuously, as expected for ruptures approaching the limiting speed in a homogeneous medium [*Rice*, 1980], but more rapidly as a result of the normal stress reduction. In contrast, at the NW front this tendency for shortening is offset by the increasing normal stress.

[29] Also shown in Figure 4d are contours of zero slip speed behind the rupture fronts. As the SE rupture front approaches $x = 200$ m, the slip velocity drops to zero behind the slip-weakening region, and a pulse of narrowing width but increasing slip velocity and total slip detaches from the front of the crack (inset). This is reminiscent of the pulses studied by *Andrews and Ben-Zion* [1997] and *Cochard and Rice* [2000], but it is spawned by the growing crack rather than by the imposed initial conditions.

[30] The variation in normal stress near the SE rupture front is shown in more detail in Figure 5. As pointed out by *Andrews and Ben-Zion* [1997], the stress change is compressive ahead of the rupture front; in all our growing crack simulations it reaches a maximum amplitude at the tip. Behind the front $\Delta\sigma_n$ rapidly becomes tensile. While the compression ahead of the front is rather modest, the maximum tensile stress grows from 10 MPa ($\sim\Delta\tau^{p-r}$) in the first snapshot to 48 MPa in the last. The bold dashed lines are estimates of $\Delta\sigma_n$ from equation (2), obtained by extracting the slip gradients from the simulations and by determining μ^* from the rupture speed and elastic properties. The difference between the estimated and computed maximum tensile stress is <8%, indicating that Weertman's steady-state solution remains a good guide to the normal stress changes behind the fronts of smoothly growing ruptures. The predicted $\Delta\sigma_n$ is zero ahead of the rupture

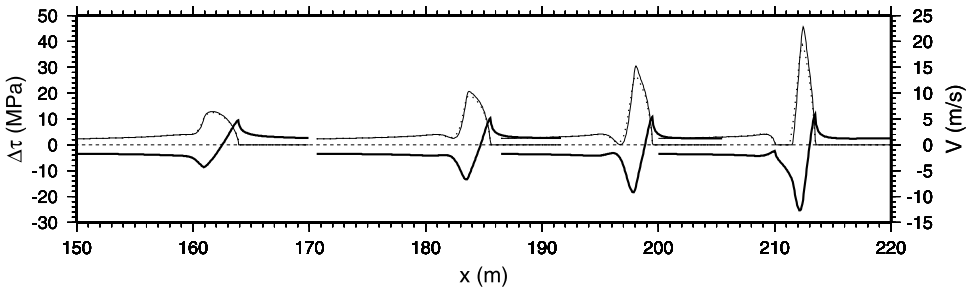

Figure 6. Slip velocities (thin lines) and shear stress changes $\Delta\tau$ (thick) for the same snapshots as in Figure 5. A slip pulse is just forming in the third snapshot and is well separated from the parent crack by the fourth. The dotted lines show the velocity profiles at 1/2 the resolution (12.5 versus 6.25 cm), suggesting that the slip pulse is well resolved.

because the slip gradients are zero. The region of large tensile $\Delta\sigma_n$ is comparable in size to the slip-weakening zone but does not shrink as much with increasing rupture speed. The insets show $\Delta\sigma_n$ (solid lines) and $\Delta\sigma_n^*$ (dotted), emphasizing that for our choice of α, v^* and δ_σ, $\Delta\sigma_n^*$ keeps pace with $\Delta\sigma_n$ in this region.

[31] Figure 6 shows snapshots of the slip velocity and $\Delta\tau$ at the same times as Figure 5. In the first snapshot a local minimum in the slip velocity has just developed; this becomes obvious by the second snapshot. By the third snapshot this minimum has dropped to zero and the pulse begins to separate from the (still growing) crack, and by the fourth the pulse is well-developed. This progression is mirrored closely by the predicted $\Delta\sigma_n$ (proportional to the local slip gradient) in Figure 5. This mirroring would be exact if the shape of the rupture front were time-invariant (in which case $\dot{\delta} = C d\delta/dx$, where C is the rupture speed), so the close correspondence is simply an indication that the rupture shape changes slowly with propagation distance. What remains to be explained is how elasticity and the adopted friction law are consistent with the observed slip gradients. In a homogeneous medium, the slip gradient behind the slip-weakening zone decreases monotonically away from the tip. Qualitatively, it appears that in the bimaterial case the shear stress drop behind the rupture front grows to be so large, owing to the normal stress reduction, that the positive slip gradient it induces near its tail end is larger in magnitude than the negative slip gradient that results from a constant stress-drop crack. This produces first a local minimum in (Figures 5a–5b) and ultimately a reversal in sign of (Figures 5c–5d) the slip gradient, which in turn generates a locally compressive $\Delta\sigma_n$ that helps lock the fault.

[32] We note that this spontaneous pulse is the one style of behavior we have encountered with subshear ruptures that is sensitive to the regularization in equation (6). For $\alpha = 1$ and $v^* = 0$ (σ_n^* evolves with slip alone) no pulse separates from the parent crack (Figure 7), at least not before the peak velocity becomes so large (roughly 200 m/s) that the evolution of σ_n^* is unresolved numerically and the simulations becomes very noisy. Apparently the pulse does not form because $\Delta\sigma_n^*$ evolves less rapidly as the slip velocity decreases from its peak, and so continues to promote slip (compare the insets in Figures 7 and 5).

3.2. Dimensional Analysis

3.2.1. Fault-Normal Stress Changes

[33] We can make a crude (under)estimate of the magnitude of $\Delta\sigma_n$ at the SE front by neglecting any feedback between normal stress variations and slip (e.g., $\sigma_n^* = \sigma_n^\infty$). Under such conditions, ruptures in our simulations would propagate with a constant fracture energy $G_c = 0.5\Delta\tau^{p-r}\delta_c$. Results from *Freund* [1990, section 6.3.3] and *Rice* [1980, section 5.5] show that for a self-similar shear crack in a homogeneous medium, the ratio of the energy release rate G to the corresponding value G_0 for a quasi-static crack decreases monotonically from 1 at zero speed to zero at the limiting speed. For a uniform stress drop, G_0 is proportional to crack length L. Thus one can infer that as L increases, the rupture speed approaches the limiting velocity more and more closely so as to maintain $G = G_c$.

[34] By treating the slip-weakening stresses behind the rupture front as if they were a steady-state feature, *Rice*

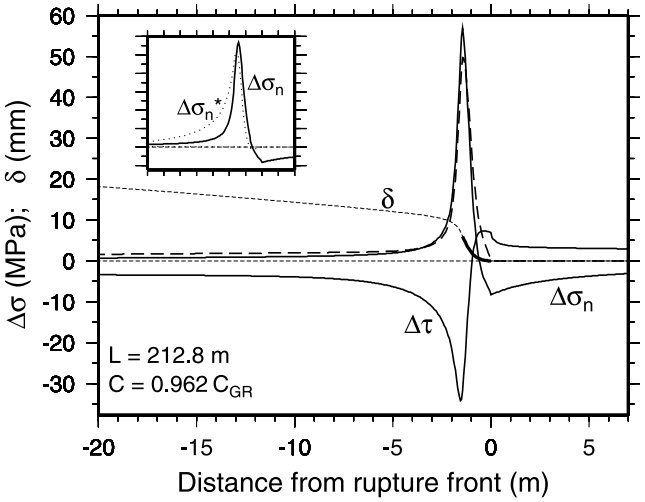

Figure 7. A snapshot of the rupture front for the same conditions as in Figure 5 but with $\alpha = 1$, $v^* = 0$, and $\delta_\sigma/\delta_c = 0.1$ (pure slip-dependent evolution of σ_n^*). No pulse forms because $\Delta\sigma_n^*$ does not track $\Delta\sigma_n$ to small values as closely, as the slip velocity decreases behind the rupture front (compare the inset to those in Figure 5).

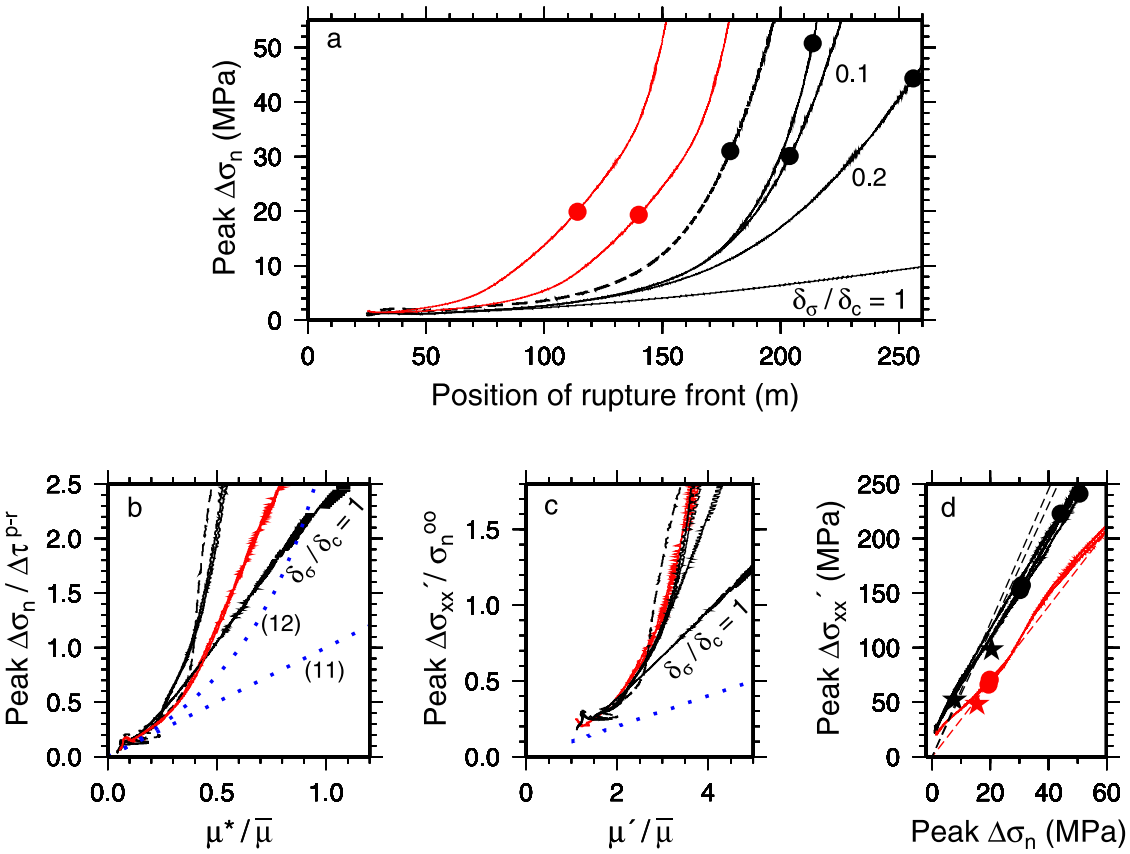

Figure 8. (a) Peak $\Delta\sigma_n$ as a function of the position of the SE rupture front, for $C_{S_2}/C_{S_1} = 1.18$ (black curves) and 1.41 (red) (dashed line is for $\rho_2/\rho_1 = 1.2$; see text for other parameters). Dots denote pulse onset. (b) Peak normalized $\Delta\sigma_n$ as a function of $\mu^*(C)/\bar{\mu}(C)$ extracted from the same simulations. Dotted lines indicate the dimensional estimates from (11) and (12). (c) Peak normalized $\Delta\sigma'_{xx}$ as a function of $\mu'/\bar{\mu}$; dotted line indicates the dimensional estimate from (14). The dimensional estimates in (11) and (14) neglect feedback between $\Delta\sigma_n$ and slip. (d) Peak $\Delta\sigma'_{xx}$ vs. peak $\Delta\sigma_n$, showing the separation into two trends based on C_{S_2}/C_{S_1}. The dashed lines show the ratio μ^*/μ', evaluated at $0.985C_{S_1}$ for $C_{S_2}/C_{S_1} = 1.41$ and $0.965C_{GR}$ for $C_{S_2}/C_{S_1} = 1.18$ (in the latter case one curve each for $\rho_2/\rho_1 = 1$ and 1.2). Dots denote pulse onset from (a); stars denote pulse onset with barriers (Figure 11 for black stars; Figure 13c for red star).

[1980] showed that the slip-weakening region shortens monotonically as the limiting speed is approached. In essence, the form of (1) shows that if some near-tip slip distribution satisfies the adopted slip-weakening law at zero velocity, then at nonzero velocity the same slip distribution compressed by the factor $\bar{\mu}/\bar{\mu}_0 = \bar{\mu}/\mu'$ also satisfies that law. Thus the ratio of the slip-weakening length R to that at zero speed R_0 is

$$\frac{R}{R_0} = \frac{\bar{\mu}}{\mu'} \ . \tag{9}$$

If we approximate the stress drop as being linear with distance behind the rupture front, as is nearly the case if the stress decreases linearly with slip, then from Rice's equation (6.12)

$$R_0 \approx \frac{9\pi}{32} \frac{\mu'}{\Delta\tau^{p-r}} \delta_c \ . \tag{10}$$

From equation (2) an average normal stress change over the slip-weakening region is $\mu^*\delta_c/R$, so from equations (9) and (10) we obtain

$$\frac{\Delta\sigma_n}{\Delta\tau^{p-r}} \approx \frac{\mu^*}{\bar{\mu}} \ . \tag{11}$$

[35] Figure 8 compares this estimate to the results of a suite of simulations with differing boundary conditions, material properties, and constitutive parameters. In all cases but two $\alpha = 0$, $v^* = 4$ m/s (time evolution of σ_n^*) and $\rho_2/\rho_1 = 1$. The black curves are for $C_{S_2}/C_{S_1} = 1.18$ and the red curves for $C_{S_2}/C_{S_1} = 1.41$. In Figure 8a the three labeled curves show that as δ_σ/δ_c is reduced from 1 to 0.2 to 0.1 (that is, as σ_n^* tracks σ_n more and more closely), $\Delta\sigma_n$ increases more and more dramatically, as expected. *Andrews and Harris* [2005] effectively use $\delta_\sigma/\delta_c = 1$, which may have contributed to the lack of a strong bimaterial effect in their simulations. Because of the instability that arises for the instantaneous response of σ_n^*, one should

not expect these curves to converge for all rupture lengths as δ_σ/δ_c decreases to zero. However, they should begin to diverge at successively larger L, as is seen here.

[36] The curve closest to that labeled 0.1 is identical except that $\alpha = 1$ and $\delta_\sigma/\delta_c = 0.2$ (σ_n^* evolves with time and slip). This is the set of parameters we typically use in simulations with barriers. Those barriers are placed closer than 160 m, where σ_n^* tracks σ closely enough that further reductions in δ_σ/δ_c would be (almost) irrelevant, but we cannot reduce δ_σ/δ_c further and still guarantee faithfulness to the underlying equations. The dashed curve is for $\rho_2/\rho_1 = 1.2$, so $\mu_2/\mu_1 = 1.68$ rather than 1.4 to maintain $C_{S_2}/C_{S_1} = 1.18$. The lower red curve is identical to the black curve labeled "0.1" except for having a larger material contrast. The larger $\Delta\sigma_n$ at the same rupture length does not justify the statement of *Shi and Ben-Zion* [2006] that bimaterial effects are reduced when C_{GR} does not exist. The upper red curve is identical to the lower except that τ_{bg} was increased to give it a 25% larger nominal stress drop.

[37] In each of these simulations, the peak value of $\Delta\sigma_n$ at each time step differs from the value estimated from the maximum slip gradient and μ^* (as in Figure 5) by less than 30%, and typically by less than 10%. Figure 8b attempts to carry this estimate one step farther, by plotting the peak value of $\Delta\sigma_n/\Delta\tau^{p-r}$ at each time step as a function of the current $\mu^*/\bar{\mu}$ (the latter ratio requires the extraction only of the rupture velocity, rather than both that velocity and the maximum slip gradient). The straight blue dotted line shows the estimate $\Delta\sigma_n/\Delta\tau^{p-r} = \mu^*/\bar{\mu}$ from equation (11). For normalized stress changes smaller than 0.2 this estimate is quite good. For larger stress changes the agreement decreases because of the feedback between the normal stress reduction and slip, which (11) neglects (the curve which deviates least has $\delta_\sigma/\delta_c = 1$, which is the value for which this feedback is least significant). One can make a first-order correction to (11) by treating the estimated $\Delta\sigma_n$ times the friction coefficient as a reduction in cohesive stress. Substituting $|\sigma_n^\infty|\Delta f + \Delta\sigma_n f$ for $\Delta\tau^{p-r}$ in (11), the estimated normal stress change becomes

$$\frac{\Delta\sigma_n}{\Delta\tau^{p-r}} \approx \frac{\mu^*}{\bar{\mu}}\left(1 - f\frac{\mu^*}{\bar{\mu}}\right)^{-1}, \tag{12}$$

where $\Delta\tau^{p-r}$ retains its original definition of $|\sigma_n^\infty|\Delta f$. This estimate (curved blue dotted line in Figure 8a) shows improved agreement with the numerical simulations. Whether one adopts (11) or (12), the extent to which the numerical curves coincide (especially neglecting the case $\delta_\sigma/\delta_c = 1$) is indicative of the extent to which the single parameter $\mu^*/\bar{\mu}$ embodies the sizeable range of material contrasts, constitutive parameters, and stress drops in Figure 8a.

[38] An obvious extension of this approach would be to derive expressions for G/G_0 as a function of rupture velocity for bimaterials. Given τ^∞, this would then allow one to estimate $\Delta\sigma_n/\Delta\tau^{p-r}$ as a function of rupture length without having to extract the rupture velocity from the simulations. The fiction of treating the near-tip shear stresses as if they were a steady-state feature of the rupture front is somewhat limiting, however; they soon become so low that if truly steady-state they would constitute a negative rather than a positive contribution to G_c. In the simulation of Figure 4 (labeled "0.1" in Figure 8a) this occurs for $L \gtrsim 180$ m.

3.2.2. Fault-Parallel Stress Changes

[39] As discussed by *Rice* [1980] for homogeneous media, the shrinking of the slip-weakening region as the rupture approaches its limiting speed leads to corresponding increases in the fault-parallel (and other) stresses near the tip that are likely to induce off-fault damage and limit the propagation speed. As a proxy for these off-fault stresses we define an approximate fault-parallel stress change $\Delta\sigma'_{xx}(x) \equiv E\epsilon_{xx}(x)$, where ϵ_{xx} is the fault-parallel strain change and E is the appropriate Young's modulus (for simplicity we do not account for the smaller change in shear stress on the fault surface when estimating $\Delta\sigma'_{xx}$). The fault-parallel stresses are not identical on the two sides of the fault (the ratio of the strains is not exactly the inverse of the ratio of the respective Young's moduli), but for a dimensional estimate it is sufficient to consider the average strain on the two sides ($\sim 0.5 d\delta/dx$) and an average Young's modulus (approximated as $2\mu'[1-\nu][1+\nu] \approx 2\mu'$), so

$$\Delta\sigma'_{xx} \approx \mu' \frac{d\delta}{dx}. \tag{13}$$

Limiting the off-fault damage entails limiting the tensile stress perturbation relative to the confining pressure. With $d\delta/dx \approx \delta_c/R$, and using (9) and (10) (which again neglect any coupling between normal stress changes and slip), the ratio of $\Delta\sigma'_{xx}$ to the ambient normal stress (a measure of the confining pressure) is

$$\frac{\Delta\sigma'_{xx}}{|\sigma_n^\infty|} \approx \Delta f \frac{\mu'}{\bar{\mu}}. \tag{14}$$

Figure 8c plots the peak $\Delta\sigma'_{xx}/|\sigma_n^\infty|$ versus $\mu'/\bar{\mu}$ for the above simulations, evaluating $\Delta\sigma'_{xx}$ on the tensile (higher modulus) side of the rupture front, and the blue dotted line indicates the slope $\Delta f = 0.1$ anticipated from (14). As with the straight blue dotted line in Figure 8b, the agreement is better for small stress changes because of the neglect of normal stress/slip coupling, but in this case the coincidence between the numerically determined curves for large stress changes is even greater.

[40] Dividing (2) by (13) yields

$$\frac{\Delta\sigma_n}{\Delta\sigma'_{xx}} \approx \frac{\mu^*}{\mu'}. \tag{15}$$

This is a useful relation because it assumes nothing about the coupling between normal stress changes and slip. Figure 8d plots the peak $\Delta\sigma'_{xx}$ (again on the higher-modulus side) versus the peak $\Delta\sigma_n$ for the same simulations. The dashed lines show the ratio μ^*/μ', evaluated at $0.985C_{S_1}$ for $C_{S_2}/C_{S_1} = 1.41$ (red) and $0.965C_{GR}$ for $C_{S_2}/C_{S_1} = 1.18$ (black); these are good average rupture speeds for the right half of the plot. Note that the curves for each ratio of C_{S_2}/C_{S_1} cluster tightly. The filled circles show that for $C_{S_2}/C_{S_1} = 1.18$ the fault-parallel stresses have reached 150–250 MPa prior to pulse formation. Given that the fault-normal stress is only 100 MPa, this is

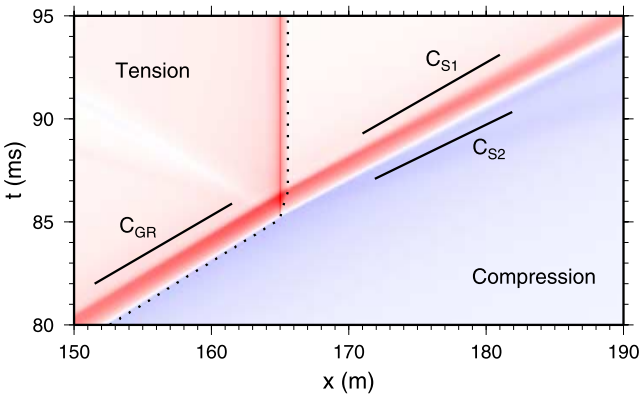

Figure 9. Space-time plot showing a rupture with the parameters of Figure 4 encountering an "unbreakable" barrier at x = 165 m. Dotted line shows the rupture front; solid lines show the indicated wave speeds. Compressive and tensile $\Delta\sigma_n$ denoted by blue and red, respectively. Until it encounters the barrier, the rupture tip coincides with the maximum compressive stress.

a clear indication that off-fault deformation will precede, and thus may supercede, pulse development. In contrast, by virtue of forming at lower values of $\Delta\sigma_n$ and having a much higher ratio of $\Delta\sigma_n/\Delta\sigma'_{xx}$, pulses develop for C_{S_2}/C_{S_1} = 1.41 by $\Delta\sigma_n$ = 70 MPa (still large, but at least less than $\bar{\sigma}_n^{\infty}$). In the next section we show that pulses arise at still lower stress levels (stars in Figure 8d) when ruptures encounter barriers.

3.3. Stopping Ruptures

[41] The simulations of section 3.1 show that $\Delta\sigma_n$ ahead of the SE front of growing ruptures is compressive. This does not appear to advance our explanation for the aftershock asymmetry, which operates most simply if the fault ahead of the rupture experiences transient tensile stresses. However, such tensile stresses are associated with rupture arrest. Figure 9 shows that if the SE rupture front of Figures 4–6 is stopped by an abrupt stress barrier $\Delta\tau_{barr}$ = −100 MPa at x = 165 m, the tensile stress behind the rupture front continues down the fault, slightly attenuated, as a dispersive wave with a velocity between C_{S_1} and C_{S_2} (not a Stoneley wave because for similar densities these interface waves exist only for exceedingly small contrasts in C_S [*Scholte*, 1947]). For barriers that are not as abrupt, this stress pulse carries a dying slip pulse with it. Because of the large shear stress concentration at the crack tip in Figure 9, slip continues for 0.5 m into the barrier. Substantial values of $\Delta\sigma_n$ persist near 165 m because of the very large slip gradients produced by the ∼100 MPa shear stress change there. The detailed evolution of $\Delta\sigma_n$ in the presence of barriers appears to be dictated by the balance between the increase due to the increasing slip gradient and the decrease due to the decreasing rupture velocity. In subsequent calculations we employ stress barriers that are not so pathologically abrupt, with the result that, unlike the example in Figure 9, the maximum tensile stress reached during any simulation is smaller than would have occurred at that distance from the origin in the absence of the barrier.

[42] For comparison purposes, in Figure 10 we show two space-time plots of ruptures encountering barriers in homogeneous media. In Figure 10a, "unbreakable" barriers as in Figure 9 have been placed at ±175 m. Slip behind the rupture fronts ceases with the arrival of the P-wave stopping phase from the opposite crack tip and briefly resumes again with the arrival of the S-wave stopping phase. In Figure 10b the barriers consist of a reduction in shear stress of 0.2 MPa/m placed symmetrically at ±175 m (and smoothed over a distance of ±4 m to avoid a kink in the stresses). In this case the rupture fronts slow gradually until the arrival of the P-wave stopping phases. Qualitatively, this behavior can be explained with reference to the results of *Freund* [1990]. As the rupture propagates further and further into the barrier, G_0 decreases so G/G_0 must increase to maintain $G = G_c$. Because for self-similar cracks G/G_0 reaches its maximum value of 1 at zero rupture velocity, we expect the crack tips to remain near failure as propagation ceases. Freund's self-similar solution does not admit slowing cracks, however, and in fact the slipped fault drops slightly below the failure

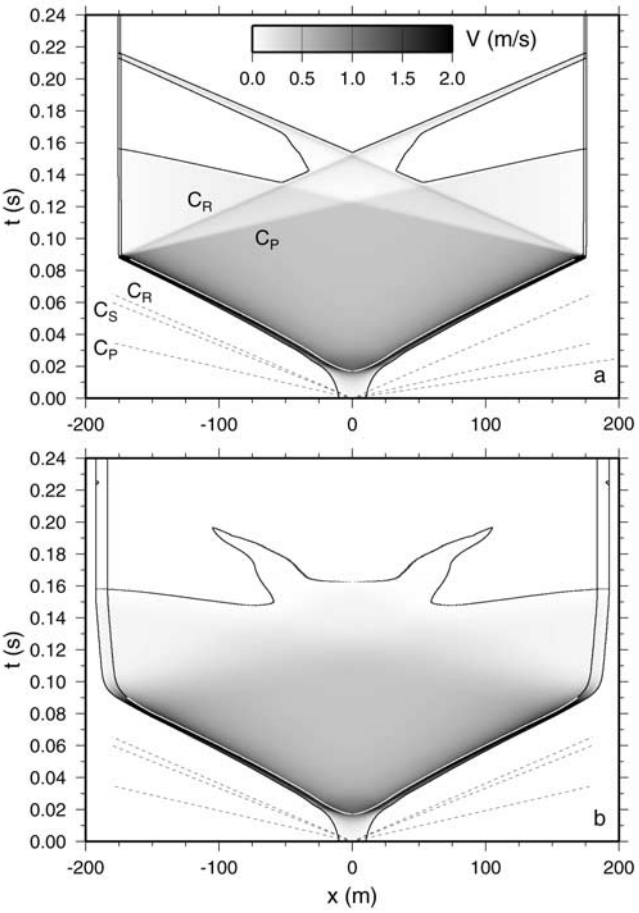

Figure 10. Space-time plots of ruptures in a homogeneous medium. Solid lines show the rupture front, tail end of the slip-weakening region (white where the slip velocity is large), and contours of zero slip speed as in Figure 4. Dashed lines show the indicated wave speeds. Grayscale image shows the slip speeds. (a) "Unbreakable" barriers placed at ±175 m. Well-defined stopping phases propagate at the P-wave and Rayleigh speeds. (b) Stress barriers of 0.2 MPa/m placed at ±175 m and smoothed over ±4 m.

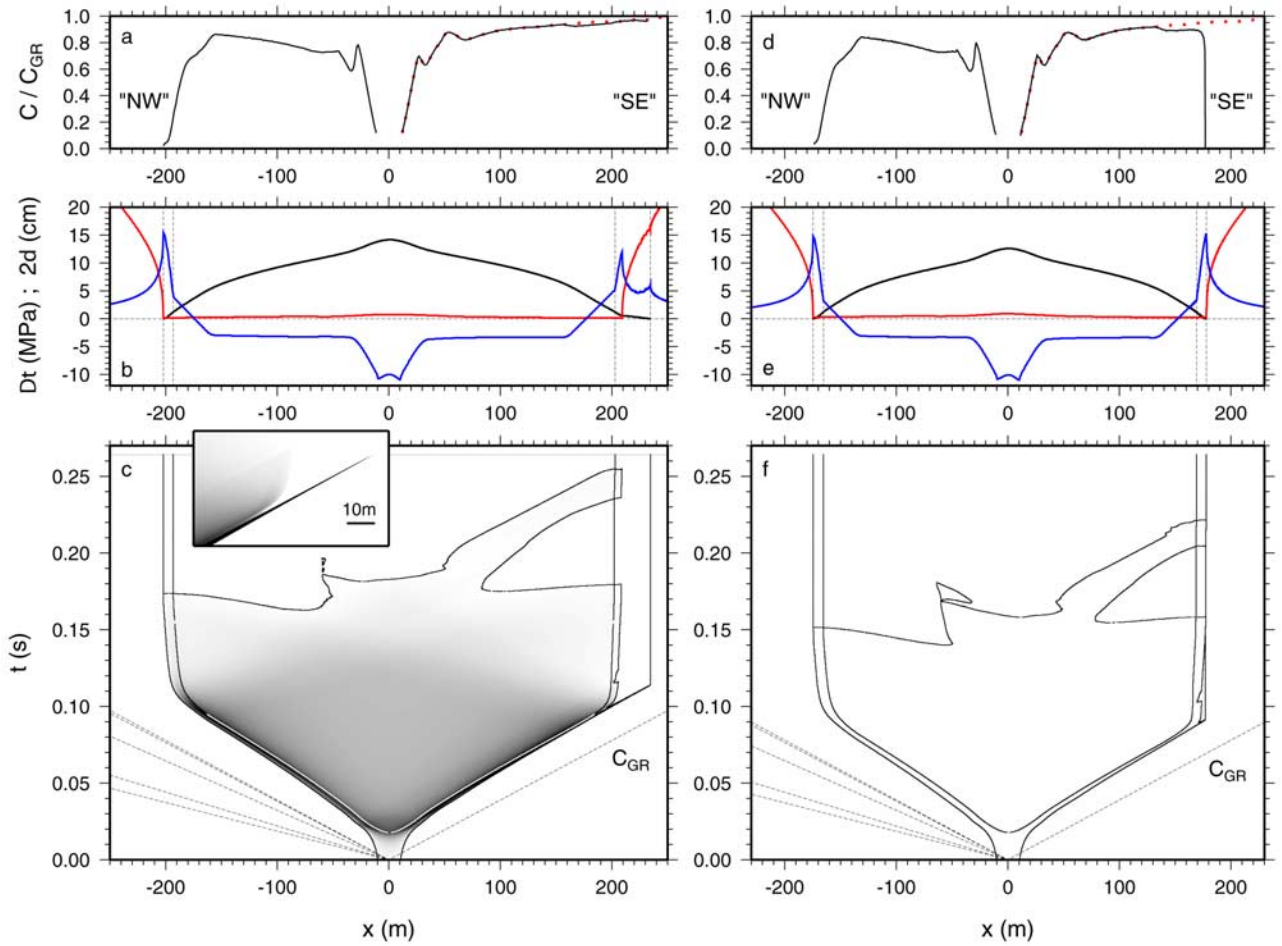

Figure 11. (a–c) Results for the conditions of Figure 4 but with $\alpha = 1$, $v^* = 4$ m/s, and $\delta_\sigma/\delta_c = 0.2$, and with the addition of shear stress barriers of 0.2 MPa/m placed at ±160 m. Velocities of the rupture fronts are shown in Figure 11a. The red dotted line shows the rupture velocity without the barrier. Shown in Figure 11b are slip δ (times 2; black line), distance from the failure envelope $-(\tau - f|\sigma_n|)$ (red line), and shear stress change $\Delta\tau$ (blue line) after the cessation of slip ($\Delta\tau$ and δ are with respect to the end of the quasi-static nucleation). Note that the slip pulse has smoothed the displacement profile over about 30 m at the SE end of the rupture, and that $-(\tau - f|\sigma_n|)$ is 16 MPa at the SE rupture tip. The form of $\Delta\tau_{nuc}$ and $\Delta\tau_{barr}$ can be seen in the shape of the blue curve near the origin and for $\delta > \delta_c$ near the rupture margins, respectively. Dashed lines bracket the slip-weakening region. Shown in Figure 11c is the space-time plot of the rupture, with a grayscale image of the slip velocity (peak velocity 10 m/s; scale saturates at 2 m/s) and solid lines as in Figure 10. Inset shows an enlargement of the pulse at the SE front. (d–f) Results for identical parameters except that the barriers have been placed at ±135 m. In this case the pulse is overridden by subsequent crack expansion. Asymmetry beyond the rupture ends is essentially nonexistent.

threshold after the passage of the stopping phases (by about 0.2 MPa at the rupture ends in Figure 10b, or about 7% of the static stress drop).

[43] Figures 11a–11c show the corresponding case for $C_{S_2}/C_{S_1} = 1.18$, with the shear stress barriers of 0.2 MPa/m located at ±160 m. Qualitatively, the NW rupture front behaves as it would in a homogeneous medium; it slows as it encounters the barrier and reaches its furthest extent with the arrival of the P-wave stopping phases. After arrest it similarly lies ~0.2 MPa below the failure threshold.

[44] At the SE front this is not the case. When the rupture front encounters the barrier, it slows slightly (Figure 11a), but the tensile stress pulse behind the front slows less. As it begins to pass the rupture front, this tensile stress pulse spawns a slip pulse that continues to propagate at nearly the no-barrier velocity before dying. The (now-diminished) stress pulse then continues on at a velocity between C_{S_1} and C_{S_2}, as in Figure 9. What does stop in a manner reminiscent of the NW rupture front is the crack-like rupture behind the SE slip pulse. This is similarly driven forward by the arrival of the stopping phases and remains very near failure after the cessation of slip. However, by this time the tensile stress that drove the slip pulse forward is long gone, and the point marking the furthest extent of rupture to the SE lies far below failure (by 16 MPa in Figure 11b). Provided the stopping phases do not move the crack-like

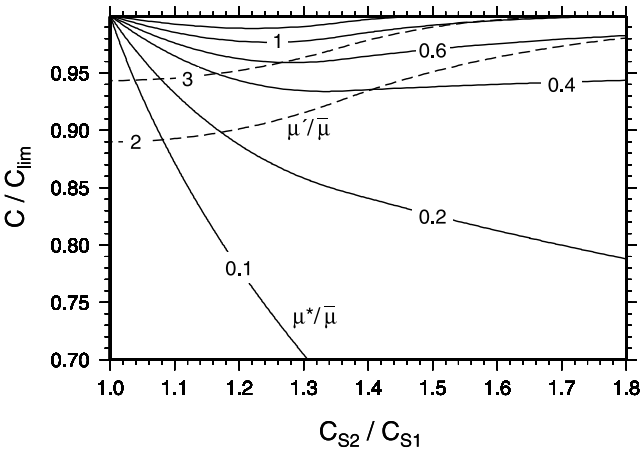

Figure 12. Contours of $\mu^*/\bar{\mu}$, a proxy for $\Delta\sigma_n/\Delta\tau^{p-r}$ (solid lines), and $\mu'/\bar{\mu}$, a proxy for $[\Delta\sigma'_{xx}/\sigma_n^{\infty}]/\Delta f$ (dashed lines), as a function of the material contrast C_{S_2}/C_{S_1} and normalized rupture speed C/C_{lim}. At constant $\Delta\sigma'_{xx}/\sigma_n^{\infty}$, $\Delta\sigma_n/\Delta\tau^{p-r}$ is expected to increase monotonically with the contrast in wave speeds.

rupture beyond the furthest extent of the slip pulse, a very asymmetric stress field results, in this example on a length scale larger than the nucleation zone.

[45] Unlike the "spontaneous" slip pulse illustrated in Figures 4–6, pulses spawned by barriers are very robust and arise equally for slip-dependence or time-dependence of σ_n^*. We can explain this in the following way: In the absence of a barrier, a tensile stress change is not a prerequisite for slip. Depending upon how quickly $\Delta\sigma_n^*$ drops back to small values behind the tip, the locally reduced shear stress may (Figure 5d) or may not (Figure 7) lead to a pulse. However, when the rupture front moves into a significant barrier, a tensile $\Delta\sigma_n$ becomes essential for slip. In the reference frame of a (previously) quasi-steady rupture front, as the ambient conditions on the underlying fault get farther and farther from failure, slip eventually can occur only where the tensile perturbation is large enough, so a pulse forms. Consistent with this view, the furthest extent of the crack-like rupture to the SE in these simulations is nearly identical to the furthest extent of the NW front, indicating that this is how far the crack could reach in the absence of normal stress changes (it progresses slightly farther to the SE because of the combination of slip during the prior pulse, which reduces the fault strength slightly, and small quasi-static normal stress changes). The pulse begins at a location slightly before the furthest extent of the crack-like rupture because this is when the spatially limited tensile perturbation becomes essential for slip (at this time the tip has not yet received all the information from the opposite end of the rupture).

[46] Although the pulse in Figure 11c forms at a much lower value of $\Delta\sigma_n$ than in the absence of a barrier (20 MPa versus 52 MPa), it falls along the same trend of $\Delta\sigma_n/\Delta\sigma'_{xx}$ in Figure 8d (upper black star) and $\Delta\sigma'_{xx}$ has reached 98 MPa by this time. This is still problematic, as it is again suggestive of large-scale off-fault deformation. This is not to say that a bimaterial effect cannot be important in the presence of such deformation, but inelastic deformation is expected to limit the rupture speed so the larger normal stress changes we compute for larger rupture speeds might never be realized. Moving the stress barriers closer to the origin reduces $\Delta\sigma'_{xx}$, but at the expense of weakening the slip pulse. If the rupture is stopped too early, $\Delta\sigma_n$ is too low for pulses to form. If it is stopped somewhat later, weak pulses are generated that are subsequently overridden by the still-growing crack. Figures 11d–11f show such an example in which the barriers of Figures 11a–11c have been moved to ±135 m. In this case the maximum values of $\Delta\sigma_n$ and $\Delta\sigma'_{xx}$, both reached slightly before pulse formation, are 7.8 and 52.1 MPa. Because the pulse is overridden by continued growth of the crack-like rupture, the final state is determined under conditions of slow growth when bimaterial effects are insignificant. In terms of the final slip distribution or distance to failure beyond the rupture ends, no asymmetry is discernible.

3.3.1. Requirements for Pulse Formation

[47] We find empirically that generation of a robust slip pulse requires that $\Delta\sigma_n$ reach a magnitude comparable to $\Delta\tau^{p-r}$. From equation (12) this corresponds to

$$\frac{\mu^*}{\bar{\mu}} \gtrsim (1+f)^{-1} \equiv Q\,, \tag{16}$$

where Q is some modest fraction of 1 (predicted to be 0.6 for $f = 0.65$, but the numerical simulations in Figure 8b suggest that $Q \sim 0.4$ may be more accurate). Because μ^* increases monotonically as the limiting rupture speed is approached while $\bar{\mu}$ decreases monotonically to zero (when C_{GR} exists) or to a small but finite value (when it does not; Figure 3a), satisfying (16) is essentially guaranteed for a constant stress-drop crack, even for arbitrarily small velocity contrasts; one need only wait long enough for the rupture to get close enough to the limiting speed. As an explanation for the aftershock asymmetry of Figure 1, this is somewhat unsatisfying, however. First, various factors might prevent C/C_{lim} from getting sufficiently close to 1, such as too heterogeneous a stress field or barriers that are too close to the nucleation site. Second, as we have already stated, rupture speeds too close to the limiting velocity imply very large off-fault stresses, which, by promoting damage, are likely to limit the rupture velocity.

[48] Because $\mu'/\bar{\mu}$ is a measure of both C/C_{lim} and the magnitude of the off-fault stresses, generating asymmetry while satisfying the above concerns requires not only that $\mu^*/\bar{\mu}$ reach some critical value Q but that it does so before $\mu'/\bar{\mu}$ becomes too large. Figure 12 shows contours of $\mu^*/\bar{\mu}$ (solid) and $\mu'/\bar{\mu}$ (dashed) as a function of the material contrast C_{S_2}/C_{S_1} and rupture speed C/C_{lim}. Figure 8b suggests $\Delta\sigma_n \gtrsim \Delta\tau^{p-r}$ requires $\mu^*/\bar{\mu} \lesssim 0.4$, and Figure 8c suggests that limiting $\Delta\sigma'_{xx}$ to (for example) $0.5|\sigma_n^{\infty}|$ requires (for $\Delta f = 0.1$) $\mu'/\bar{\mu} \lesssim 2.5$. Although the indicated values for these ratios were derived from simulations without barriers, Figure 12 is nonetheless sufficient to show that if the goal is to maximize asymmetry ($\mu^*/\bar{\mu}$) while limiting the off-fault stresses ($\mu'/\bar{\mu}$), this may be achieved either by increasing the velocity contrast or (from equation (14)) by decreasing Δf. Figures 13a–13c show results for $C_{S_2}/C_{S_1} = 1.41$, using parameters that are otherwise identical to those in Figure 11. For velocity contrasts

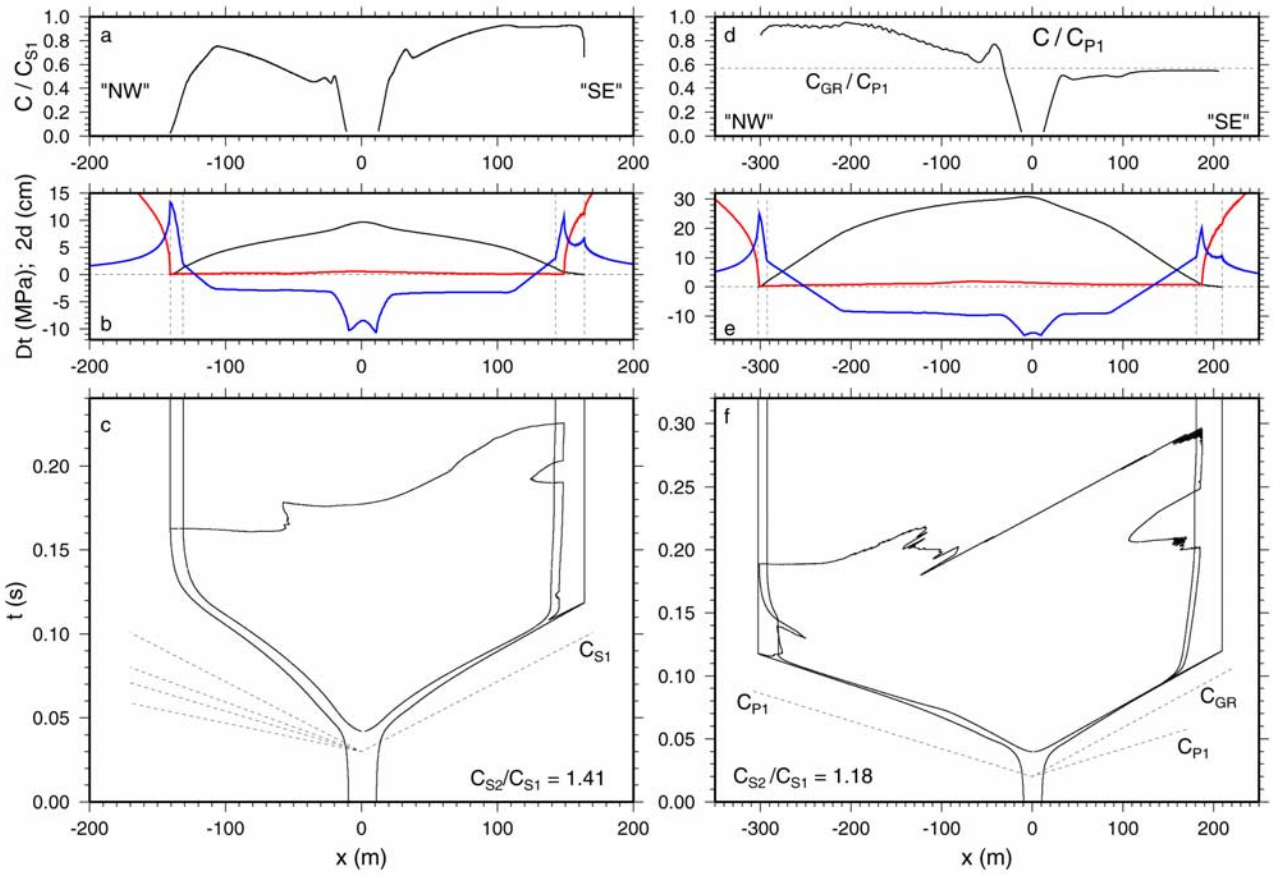

Figure 13. (a–c) Results for the conditions of Figure 11 but with $C_{S_2}/C_{S_1} = 1.41$ ($C_{S_1} = 2400$ m/s) and barriers placed at ±110 m. For velocity contrasts this large C_{GR} does not exist and the limiting rupture speed is C_{S_1}. (d–f) Results for the conditions of Figure 11 but with $f_d = 0.55$, $\delta_c = 9$ mm, $\delta_\sigma/\delta_c = 0.1$, and $\alpha = 0$, resulting in propagation speeds approaching C_{P_1} at the NW front. Barriers of 0.2 MPa/m have been placed at 85 and −210 m. The slip pulse at the NW margin is nearly overridden by the subsequent crack-like growth.

this large C_{GR} does not exist (Figure 3a). With barriers placed at ±110 m significant asymmetry is achieved while limiting the peak $\Delta\sigma'_{xx}$ to only 49 MPa, roughly $0.5|\sigma_n^\infty|$.

[49] Results for $C_{S_2}/C_{S_1} = 1.18$ and 1.41 are further compared in Figure 14, which shows the maximum values of $\Delta\sigma_n$ (behind the rupture front) and $\Delta\sigma'_{xx}$ (on the tensile side) as a function of the position of both the NW and SE front, with barriers placed at various distances from the origin. For each ratio of C_{S_2}/C_{S_1} the curve with the largest amplitude corresponds to either Figure 11c or 13c (strong asymmetry), while the two with the smallest amplitude bracket the symmetry/asymmetry transition (distinguished by whether or not the slip pulse is later overrun by the crack-like rupture front). In both cases the symmetry/asymmetry transition occurs for peak values of $\Delta\sigma_n$ within a few tens of percent of $\Delta\tau^{p-r}$, but for $C_{S_2}/C_{S_1} = 1.41$ significant asymmetry is achieved with much lower values of $\Delta\sigma'_{xx}$.

[50] These and other simulations are summarized in Figure 15, where Figures 15a–15c show various measures of asymmetry as a function of the maximum $\Delta\sigma_n$ reached. Red, black, and green symbols correspond to $C_{S_2}/C_{S_1} = 1.41$, 1.18, and 1.10, respectively. The different symbol shapes encompass stress barriers of 0.1, 0.2, and 0.4 MPa/m; peak-residual strength drops $\Delta\tau^{p-r}$ of 5, 10, and 15 MPa; nominal stress drops $(\tau_{bg} - \tau_d)/\Delta\tau^{p-r}$ of 0.28–0.52, pure time- and mixed slip- and time-dependent evolution of σ_n^*, and subshear and supershear propagation of the NW rupture front. For each set of parameters (symbols), symmetric barriers have been placed at various distances from the origin and, as in Figure 14, the two closest distances/lowest $\Delta\sigma_n$ values bracket the symmetry/asymmetry transition.

[51] It is noteworthy that the different simulations collapse to such tight trends in these plots, with the symmetry/asymmetry transition occurring for peak values of $\Delta\sigma_n/\Delta\tau^{p-r}$ of ~0.7–1. It is not obvious that this should be the case. In particular, since the working definition of the symmetry/asymmetry transition is a slip pulse that outruns the crack-like rupture to follow, one might expect that the extent of crack expansion following pulse detachment is an essential part of this story. From the self-similar results of *Freund* [1990], the amount the crack expands after encountering the barriers should increase with the ratio G_0/G_c. This implies that crack should expand more as C_{S_2}/C_{S_1} decreases because longer propagation distances are required to reach the same $\Delta\sigma_n$ (Figure 8a). For example, comparing the

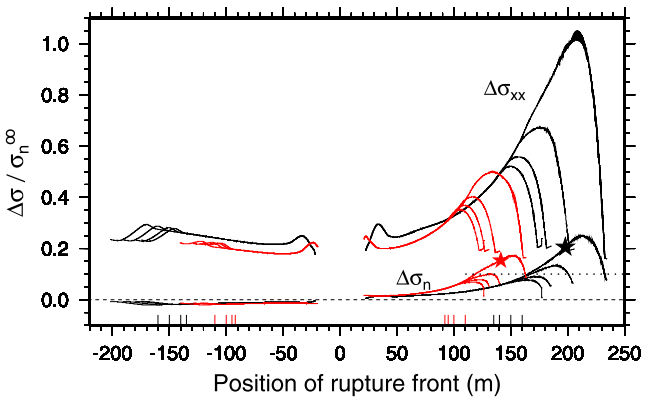

Figure 14. Normalized peak values of $\Delta\sigma'_{xx}$ (upper curves) and $\Delta\sigma_n$ (lower curves) for simulations with the conditions of Figure 11 (C_{S_2}/C_{S_1} = 1.18; black) and Figures 13a–13c (C_{S_2}/C_{S_1} = 1.41; red). Symmetric stress barriers have been placed as indicated by the tic marks on the horizontal axis. For both sets of curves, the two with the smallest stress changes straddle the asymmetry/no asymmetry transition. Stars for the curves with the largest stress change denote pulse onset. The normalized value of $\Delta\tau^{p-r}$ here is 0.1 (dotted line in lower right). The larger material contrast produces significant asymmetry with much smaller off-fault stresses.

green and red filled circles in Figure 15, which differ only in C_{S_2}/C_{S_1}, the barriers at the symmetry/asymmetry transition are located at ~90 m for C_{S_2}/C_{S_1} = 1.41 and ~250 m for C_{S_2}/C_{S_1} = 1.10. This factor of ~2.8 difference in crack size results in a factor of ~2.8 difference in G_0. By treating the barriers as an "effective" slip weakening stress, one can use equation (10) and the relation $G_c = 0.5\delta_c\Delta\tau^{p-r}$ to estimate that the distances the cracks should propagate into the barriers differ by the factor $(2.8)^{1/3} \approx 1.4$, a difference which in absolute terms is larger than the distance the pulses at the symmetry/asymmetry transition travel (see, for example, Figures 11e and 11f). In fact, there does appear to be a systematic increase in the critical $\Delta\sigma_n/\Delta\tau^{p-r}$ with decreasing velocity contrast, but it is very slight (~0.73, 0.80, and 0.84 for C_{S_2}/C_{S_1} = 1.41, 1.18, and 1.10, respectively).

[52] Figure 15d shows that the peak normalized $\Delta\sigma'_{xx}$ reached as a function of peak normalized $\Delta\sigma_n$ separate into different trends on the basis of C_{S_2}/C_{S_1}, as in Figure 8d. Comparable values of $\Delta\sigma_n$ imply much smaller $\Delta\sigma'_{xx}$ for larger velocity contrasts. The different trends extrapolate to very near the same value in the lower left corner of the plot, corresponding closely to the quasi-static values of the two parameters.

3.3.2. Supershear Rupture Fronts

[53] The black crosses in Figure 15 correspond to the same parameters as in Figure 11 but with f_d = 0.55 (so $\Delta\tau^{p-r}$ = 15 MPa) and δ_c = 9 mm (we were also forced to use pure time-dependent evolution of σ_n^*, to ensure adequate resolution in the face of quite large slip velocities at the SE front). The larger stress drop $(\tau^\infty - \tau_d)/\Delta\tau^{p-r}$ = 0.52 in this case quickly leads to supershear rupture speeds at the NW front. Qualitatively, this result is consistent with the laboratory experiments of *Xia et al.* [2005], who could reproducibly generate bilateral ruptures with supershear fronts moving in the negative direction when they increased $\tau^\infty/|\sigma_n^\infty|$ (although they observed an abrupt jump from velocities near C_{GR} to near C_{P_1}, while our transition is gradual).

[54] As the NW front becomes supershear, the normal stress change behind the front flips sign and becomes tensile. As at the SE front, when this $\Delta\sigma_n$ becomes large enough it is capable of generating a robust slip pulse. However, a much greater propagation distance is required to reach the critical $\Delta\sigma_n$, at least in part because the slip gradients behind the supershear front are smaller. For symmetric barriers at ±80 m, corresponding to the black cross with the largest $\Delta\sigma_n$ in Figure 15, the peak $\Delta\sigma_n$ behind the NW rupture front (3.9 MPa) is still too small for pulses to form. Figures 13d–13f show an example for the same parameters where barriers of 0.2 MPa/m have been placed at +85 m and −210 m. In this case pulses are generated at both the NW and SE margins; however, that to the NW is relatively weak (peak $\Delta\sigma_n$ = 14 MPa, compared to 40 MPa at the SE front). Thus the existence of supershear ruptures does not alter the expected sense of aftershock asymmetry. Because $\Delta\sigma_n$ increases so much more slowly at the NW rupture front, unless nucleation consistently occurs far closer to the SE barrier the region to the SE will continue to lie farther from failure than the region to the NW.

4. Discussion

4.1. Mechanisms of Aftershock Asymmetry

[55] In principle, the observed aftershock asymmetry could be due to asymmetry in either the time-dependent or residual (quasi-static) stress field. Figure 16 shows the time-dependent changes in shear, normal, and Coulomb failure stress $\Delta CFS = \Delta\tau + f_s\Delta\sigma_n$ at 1 gridpoint (0.125 m), 10 m, 50 m, and 150 m from each rupture end in Figure 13c. Figure 16b illustrates the decay of the tensile stress pulse as it propagates down the fault, and the subsequent approach to $\Delta\sigma_n$ = 0. Thus the "quasi-static" ΔCFS at ~0.4 s in Figure 16c is essentially $\Delta\tau$.

4.1.1. Static Stress Field

[56] Figures 11 (left) and 13 suggest two ways in which the static stress field could lead to the asymmetric distribution of aftershocks. First, note that regions beyond the rupture ends have not contributed to the rupture history and thus can take on any stress level provided that level would not previously have allowed slip. However, stresses are likely to be correlated on short length scales, so it must be regarded as significant that in these simulations the NW rupture front lies very close to the failure threshold while the SE front can lie below failure by more than $\Delta\tau^{p-r}$. Little is known of the length scales on which fault stresses are correlated, although for rate-and-state friction there are physical reasons to expect that stress variations on length scales less than the nucleation length are damped [e.g., *Rice and Ruina* 1983].

[57] Second, in the limit that on these spatial scales the ambient fault stresses are uncorrelated, one can estimate seismicity rate changes from the work of *Dieterich* [1994], at least in the context of a particular incarnation of rate-and-state friction. A static shear stress change $\Delta\tau$ is expected to give rise to an instantaneous earthquake rate increase of

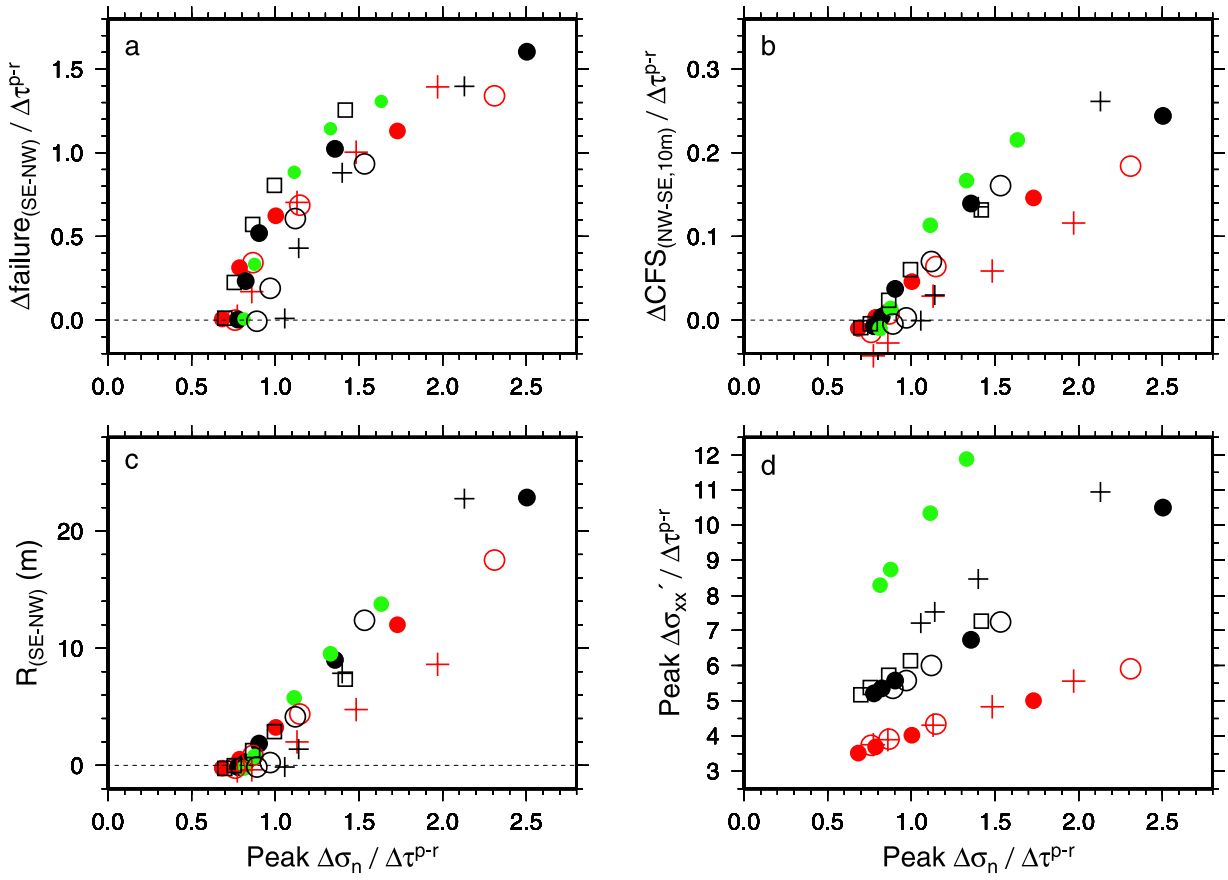

Figure 15. Various measures of the residual (quasi-static) asymmetry as a function of the peak normalized Δ_{σ_n}. Red symbols show $C_{S_2} / C_{S_1} = 1.41$; black symbols show $C_{S_2} / C_{S_1} = 1.18$; green symbols show $C_{S_2} / C_{S_1} = 1.10$. Identical symbols differ only in the placement of the symmetric stress barriers. Filled circles correspond to the "standard" parameters listed at the head of section 3, with $\Delta\tau_{barr} = 0.2$ MPa/m (as in Figures 11c, 11f, and 13c). Open black squares and circles are for $\Delta\tau_{barr} = 0.4$ and 0.1 MPa/m. Black crosses are for the conditions of Figure 13f ($\Delta\tau^{p-r} = 15$ MPa) but with symmetric barriers. Open red circles are for a stress drop 20% larger than for the red filled circles (by virtue of a greater τ_{bg}). Red crosses are for $\Delta\tau^{p-r} = 5$ MPa ($f_d = 0.65$, with δ_c also reduced by a factor of 2, and τ_{bg} increased to maintain the same ratio $(\tau_{bg} - \tau_d)/\Delta\tau^{p-r}$ as for the filled circles). (a) The distance from failure $-(\tau - f|\sigma|)$ at the SE edge of the rupture (the most distant gridpoint to slip) minus that at the NW edge, normalized by $\Delta\tau^{p-r}$. (b) The normalized difference in static Coulomb stress change $\Delta\tau + f_s\Delta\sigma_n$, 10 m beyond the rupture ends (NW-SE). (c) The difference in final length R of the slip-weakening zone (SE-NW). (d) Maximum normalized $\Delta\sigma'_{xx}$ vs. maximum normalized $\Delta\sigma_n$.

exp[$\Delta\tau/a\sigma_n$], where a (~0.01 in the lab) determines the magnitude of the direct velocity effect in the friction law. The solid lines in Figure 17a show the time-dependent seismicity rate change 10, 50, and 150 m from the NW (thick lines) and SE (thin) rupture edges, computed assuming instantaneous application of the final (static) shear stress changes in Figure 16 and using $a\sigma_n = 0.4$ MPa. Differences in seismicity rate to the NW and SE as large as those seen in Figure 1 are restricted to distances less than 50 m. At 10 m the difference is 30 times larger than that in Figure 1, but because of a factor-of-two or so uncertainty in the mainshock size it is entirely plausible that the actual asymmetry in our catalog is both larger in magnitude and more restricted spatially than we infer. In none of our simulations have we produced a large stress asymmetry as far as one rupture radius from the rupture margins. For example, the difference in quasi-static ΔCFS of 0.04 MPa at 150 m in Figure 16 would give rise to a seismicity rate difference of only 10% for $a\sigma$ = 0.4 MPa; a factor of 2 difference in seismicity rate at this distance would require $a\sigma$ to be 10 times smaller.

[58] We can compare these results to Figure 1 by integrating the pointwise seismicity rate changes from 1 to 2 radii (Figure 17b). Because our catalog is so dominated by horizontal lineations of earthquakes [*Rubin*, 2002b, Figure 7b], there is little need to correct for the increasing fault area (greater number of nucleation sites) with increasing distance in this exercise. For simplicity we just average the rate changes at distances $(n + 1/2)L_{nuc}$ beyond the rupture ends, for n an integer from 0 to $L/L_{nuc} - 1/2$, where L is the rupture half-length. A comparison of Figures 17a–17b shows that due to the exponential dependence on the stress change, the predicted asymmetry is dominated by that at small distances. The cumulative

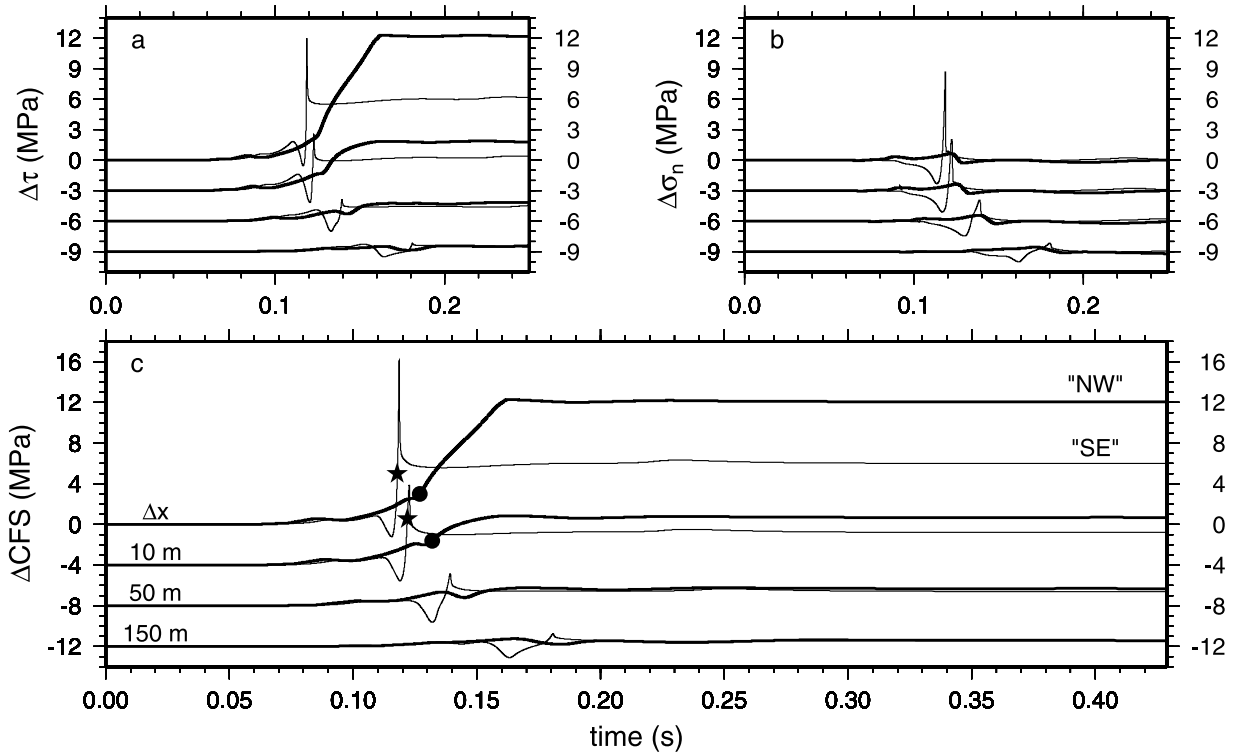

Figure 16. Time history of (a) $\Delta\tau$, (b) $\Delta\sigma_n$, and (c) $\Delta CFS = \Delta\tau + f\Delta\sigma_n$, for the simulation of Figure 13c, at distances of 1 gridpoint (0.125 m), 10 m, 50 m, and 150 m beyond the NW (thick lines) and SE (thin lines) ends of the rupture. At 0.125 m the peak ΔCFS is larger to the SE than to the NW because the rupture front has progressed farther into the barrier. Stars and circles in Figure 16c denote when the rupture front would have arrived at the indicated distances in the absence of barriers.

difference for delays up to 10 hours (a factor of 2.5) is essentially the same as that in Figure 1, but for reasons unknown the observed asymmetry extends well down the $\sim$time^{-1} portion of the seismicity rate curve, while the predicted asymmetry is restricted largely to earlier times.

4.1.2. Dynamic Stress Field

[59] A third explanation for the aftershock asymmetry is that the tensile stress pulse that runs to the SE makes nucleation sites that might otherwise have become an aftershock part of the mainshock. The dashed lines in Figure 17a show the aftershock rate computed using the time-dependent normal and shear stress changes in Figure 16 (Appendix B). The difference between the solid and dashed lines is a direct indication of the effectiveness of the time-dependent portion of the stressing history in diminishing the subsequent aftershock rate. In these calculations we assume instantaneous response of the frictional strength to changes in normal stress ($\alpha = 0$ in the notation of *Dieterich* [1994]); this maximizes the ability of the tensile stress pulse to generate earthquakes. We also neglect the fact that the tensile pulse has a smaller spatial extent than the nucleation zone. Nonetheless, the duration of the pulse is so short that the time-dependent portion of the stressing rate does not significantly effect the longer-term aftershock rate, and to the extent that it does so it seems to reduce the rate to the NW by more than that to the SE. Thus provided we are using an appropriate value for $a\sigma$, it seems much more likely to be the asymmetry in the static field that is responsible for the asymmetry of these near-source aftershocks.

4.2. Reasonable Velocity Contrasts

[60] To generate significant stress asymmetry while minimizing the off-fault stresses appears to require substantial velocity contrasts across the fault ($\gtrsim$20%, for $\Delta f = 0.1$, to keep $\Delta\sigma'_{xx} \lesssim 0.5|\sigma_n^{\infty}|$). P-wave velocity contrasts of $\sim$10–20% have been inferred from large-scale tomographic images of this section of the San Andreas fault [*Eberhart-Phillips and Michael*, 1998], and the azimuthal dependence of our own pair-wise arrival-time differences for these earthquakes indicates P-wave contrasts of $\sim$12–24%. Each of these techniques is likely to be sensitive to the across-fault velocity contrast on a relatively large length scale, however [*Rubin*, 2002a]. A more targeted approach for determining the contrast is from the move-out of head waves, relative to the direct P-wave arrivals, as seen by stations near the fault on the side with the lower wave speed. *McGuire and Ben-Zion* [2005] made such measurements for earthquakes within the Bear Valley section of the San Andreas fault, within a few kilometers of much of the region contributing to our catalogue. They obtained P-wave velocity contrasts in two locations, each averaged over $\sim$5 km along the fault, of 20% and 35%. Even these measurements were made using predominantly $\sim$10 Hz waves, with wavelengths of roughly 500 m. Because host-rock damage typically decreases with distance from major faults [*Chester et al.*, 1993], the measurements of McGuire

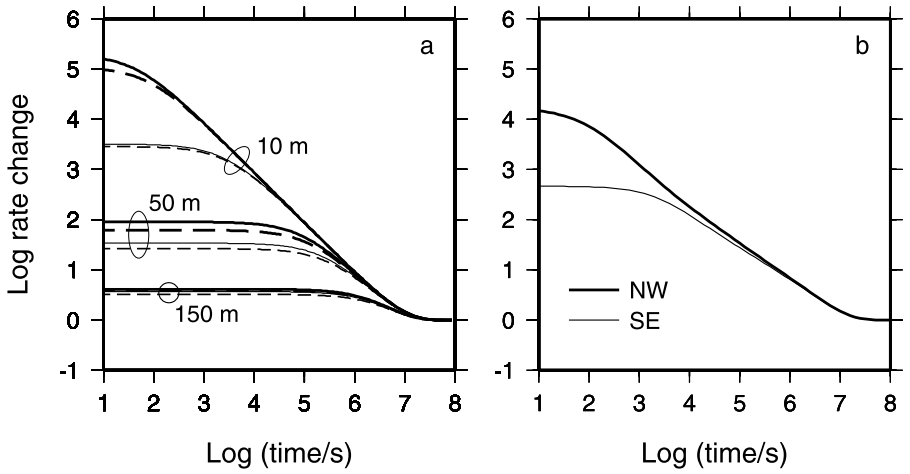

Figure 17. (a) Solid lines show computed seismicity rate change following the application of the final (quasi-static) shear stress changes in Figure 16a, at distances of 10, 50, and 150 m beyond the NW (thick lines) and SE (thin lines) ends of the rupture, using the equations of *Dieterich* [1994] and $a\sigma_n$ = 0.4 MPa. Dashed lines show seismicity rate changes computed using the full time-dependent normal and shear stress changes in Figure 16, from Appendix B. (b) "Integrated" seismicity rate change for the same simulation from 1 to 2 radii to the NW and SE. See text for discussion.

and Ben-Zion might still be underestimating the velocity contrast sensed by the earthquakes, which have an estimated median diameter of less than 100 m (and the most relevant length scale might be that of the much smaller slip-weakening region). Of course, the important contrast is that for S-waves, but this has proven to be more difficult to determine.

4.3. Aftershock Asymmetry Without Rupture Directivity?

[61] Given the ongoing discussion concerning the importance of unidirectional ruptures on bimaterial interfaces [e.g., *Harris and Day*, 2005; *Andrews and Harris*, 2005; *Dor et al.*, 2006; *Shi and Ben-Zion*, 2006], it is worth pointing out that in the model presented here the observed aftershock asymmetry results from "macroscopically" nearly symmetric ruptures, with propagation velocities to the SE that are larger by a few tens of percent or less. It is reasonable to presume that the SE rupture front, because of the associated tensile stress perturbation, might break through more barriers than the NW front, occasionally giving rise to clearly asymmetric ruptures. Simulations with differing degrees of heterogeneity may be required to test for this (it is generally accepted that heterogeneous prestress or strength can give rise to more pulse-like behavior in homogeneous media [e.g., *Oglesby and Day* 2002]).

4.4. Damage Asymmetry Without Rupture Directivity?

[62] Figure 14 shows that the maximum $\Delta\sigma'_{xx}$ near the NW rupture front is much smaller than that at the SE front. Here a negative feedback is operating, in which the compressive stress behind the NW rupture front increases with rupture velocity, with the result that the shear stress drop decreases as the rupture velocity increases. For this reason the fault-parallel strain increases only slowly with propagation distance. At least for the distance range we have modeled, $\Delta\sigma'_{xx}$ near the NW front of a subshear rupture never gets much larger than its quasi-static value. Thus observations of damage being concentrated consistently on one side of the fault [*Dor et al.*, 2005, 2006] could be indicative of a bimaterial effect without necessarily being indicative of predominantly unidirectional ruptures (although this question becomes complicated if the velocity contrast at the location of the observed damage, typically near the surface, is not representative of that controlling the rupture speed).

4.5. Other Observables?

[63] Figure 16 is suggestive of a significant NW/SE asymmetry in the timescale for potential rupture-stopping barriers to experience their peak stress. The stars and circles in Figure 16c show when the rupture front reached the gridpoint in question in a simulation with no stress barrier. From this time a barrier within 10 m of the NW rupture end has ~30 ms to "decide" if it is going to become part of the rupture (close to the time for the P stopping phase to arrive from the opposite crack tip). This suggests that if the barrier ultimately fails, it might be clearly detectable as a subevent in the waveforms. In contrast, a barrier within 10 m of the SE front has roughly 0.8 ms to make up its mind, basically the time for the passage of a 2-m tensile pulse moving at near the shear wave speed. If it fails in that time, it is unlikely to be distinguishable from continued steady propagation of the SE rupture front.

[64] *Rubin and Gillard* [2000] measured pulse widths on a suite of 72 similar M0.6–3.6 earthquakes to search for rupture directivity, and identified 5 M > 2 events that were clearly compound. These were characterized by double arrivals at stations to the SE but not at stations to the NW (starred earthquakes in Figure 18), indicating that the second subevent occurred to the NW of the first. While Rubin and Gillard interpreted this just as evidence of "very early" aftershock asymmetry, qualitatively similar to that in Figure 1, in retrospect Figure 16c provides a much more appealing explanation. That is, the fact that the pulse widths for these earthquakes are not anomalous at stations to the

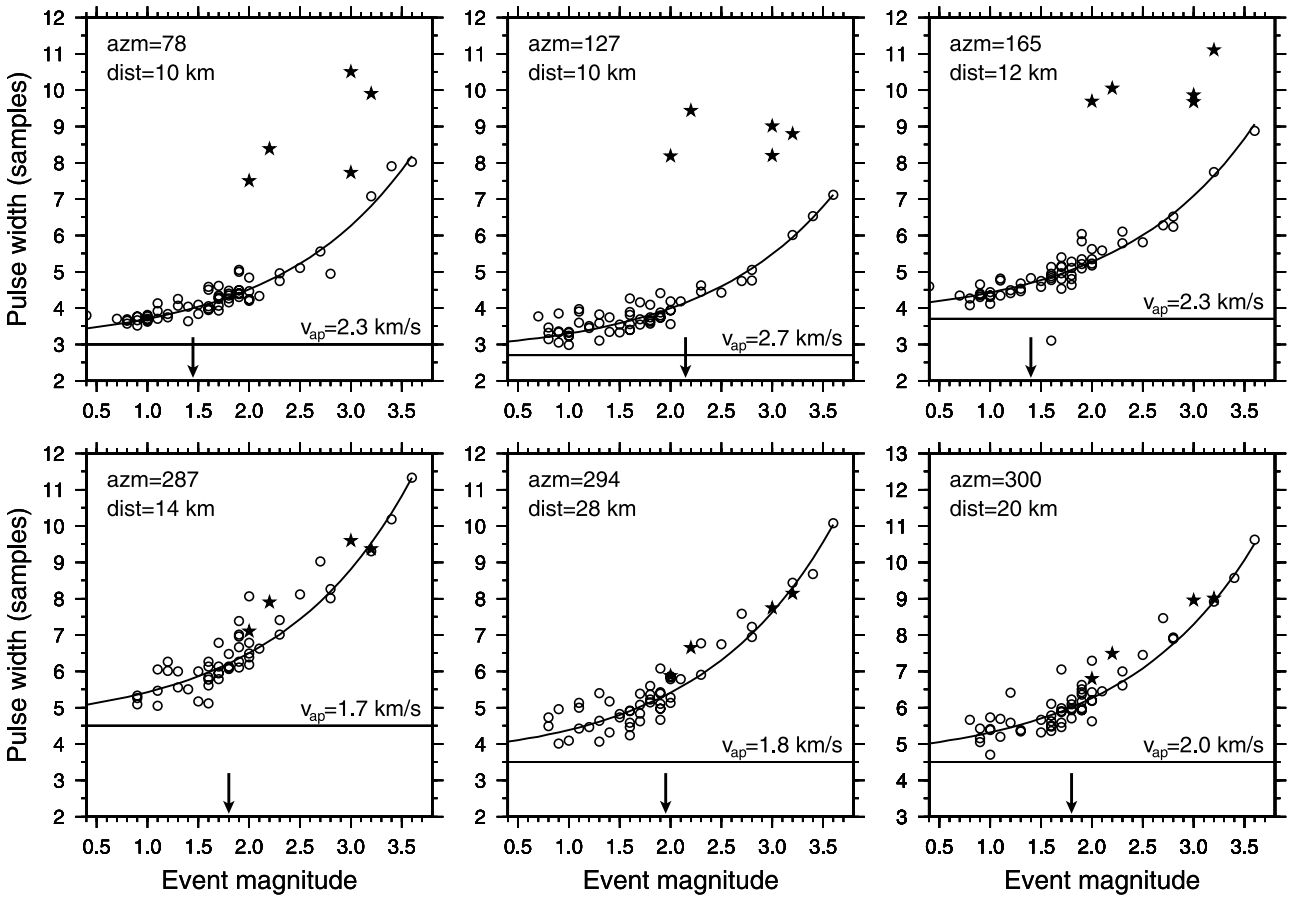

Figure 18. P-wave pulse widths as a function of magnitude, for a set of 72 similar earthquakes at three stations to the SE (top row) and NW (bottom row). Stars denote events showing a clear double arrival at stations to the SE. Curves are a two-parameter fit following Frankel and Kanamori [1983], consisting of the pulse width for a hypothetical delta function source (horizontal line) and an apparent rupture velocity (indicated, assuming circular ruptures with a 5-MPa stress drop). Arrows denote the onset of clipping. Modified from *Rubin and Gillard* [2000].

NW suggests that they are occurring on dynamic timescales. The asymmetry arises because any corresponding barriers to the SE that might have failed would have done so on a timescale that made them indiscernible at all azimuths. (The data also indicate a lesser amount of pulse widening with increasing earthquake magnitude at stations to the SE. This is suggestive of preferential propagation to the SE, but this has not been modeled quantitatively.)

4.6. Other Physics?

4.6.1. Rate-and-State Friction

[65] In Figure 17 we used a simplified rate-and-state friction model to interpret the results of a slip-weakening calculation. It would be preferable to do this in a self-consistent fashion. Previously, we ran rate-and-state simulations of dynamic ruptures on a bimaterial interface but using the "aging" or "slowness" version of the state evolution equation that we now understand to be a poor descriptor of nucleation [*Rubin and Ampuero*, 2005]. Rate-and-state ruptures obeying the aging law appear very similar to suitably-scaled slip-weakening ruptures (with $\Delta\tau^{p-r} \approx b\sigma \ln[V_{dyn}/V_{bg}]$ and $\delta_c \approx D_c \ln[V_{dyn}/V_{bg}]$, where V_{dyn} and V_{bg} are representative dynamic and background slip velocities, D_c is the slip scale for the evolution of the state variable, and b scales the magnitude of state-dependent part of the frictional strength). For this reason it is not surprising that the rate-and-state simulations shared the property that values of $\Delta\sigma_n$ approaching $\Delta\tau^{p-r}$ were required to generate robust slip pulses that outran the crack-like expansion of the SE rupture front. Unlike the slip-weakening models, however, for ratios of the static stress drop to $\Delta\tau^{p-r}$ similar to those we employed (implying $a/b \sim 0.75$ in the rate-and-state formulation), the nucleation length under the aging-law version of rate-and-state friction is many times the length of the slip-weakening-like zone behind the rupture front. It is the large ratio of δ_c/D_c under the aging law that leads to the large nucleation sizes, and that is inconsistent with laboratory experiments. Future simulations should be carried out using the "slip" law.

[66] One assumption underlying the interpretation of our simulations is that ruptures nucleate more-or-less randomly between the barriers that ultimately stop the rupture. In our quasi-static rate-and-state simulations the nucleation zone showed a strong tendency to migrate to the SE, at least while the velocity within it was not markedly larger than that outside. Whether mainshock nucleation properties

could play a role in aftershock asymmetry also needs to be explored using a rate-and-state model.

4.6.2. Three-Dimensional Effects and Stress Heterogeneity

[67] *Andrews and Harris* [2005] suggest that slip pulses are unlikely to be important in three dimensions and in the face of stress heterogeneity on the fault. Because the slip pulses we are modeling are smaller than the rupture radii by nearly a factor of 100 (essentially the ratio of the slip-weakening region to the rupture radius), we do not expect 3-D effects to be important in pulse formation; in the reference frame of the nascent pulse deformation appears 2-D. Three-dimensional effects might reduce the propagation distance of those pulses that travel the farthest in our calculations ($\sim$20% of the rupture radius). The critical $\Delta\sigma_n/\Delta\tau^{p-r}$ for generating asymmetry might be reduced in 3-D because the stopping phases will be weaker, but we do not expect this difference to be large. It should be borne in mind, however, that the geometry of any stress barriers that ultimately stop the rupture would necessarily be more complex in 3-D than in 2-D.

[68] Stress heterogeneity seems more likely to exert a controlling influence on pulse formation. On the basis of Figure 15, the critical issue would seem to be the magnitude of $\Delta\sigma_n$ (from an energy balance standpoint it might be preferable to devise a criterion where this stress magnitude is multiplied by a slip distance, but qualitatively this appears to be already accounted for in that the spatial dimension of the tensile stress pulse is closely tied to that of the slip weakening zone). If, by repeatedly slowing the rupture front, the heterogeneity prevents $\Delta\sigma_n$ from approaching $\Delta\tau^{p-r}$, then we would not expect robust pulses to form. We cannot estimate $\Delta\sigma_n$ directly from the results presented by Andrews and Harris, but in their 3-D heterogeneous case (their Figure 2) the rupture speed was apparently limited to less than two-thirds C_{GR} (but note that this might have been due to their use of a relatively large δ_σ/δ_c, as well as to heterogeneity). As their 20% material contrast was close to ours, this suggests that the criterion for sufficiently large $\Delta\sigma_n$ was not reached.

4.6.3. Inelastic Deformation

[69] To account for the inelastic deformation that is expected as the limiting rupture speed is approached, *Andrews* [2005] and *Ben-Zion and Shi* [2005] have run models that explicitly incorporate off-fault Coulomb plasticity (the former for crack-like ruptures in a homogeneous medium; the latter for slip pulses in a bimaterial with constant friction). *Andrews* [2005] found that this resulted in a damage zone size and fracture energy that increased roughly linearly with rupture length, and a propagation velocity that if not quasi-constant, at least approached the limiting speed much less rapidly than for a purely elastic calculation. The fault-normal stress change within the slip-weakening region was tensile and reached a maximum of roughly $0.5\Delta\tau^{p-r}$, presumably due to damage being dominated by fault-parallel stretching on the tensile side of the rupture front. As our models do not include off-fault deformation, we conservatively asked that significant asymmetry arise while limiting $\Delta\sigma'_{xx}$ to (rather arbitrarily) $0.5|\sigma_n^\infty|$. It is possible that this is too conservative, as the normal stress reduction that Andrews found might augment the purely elastic bimaterial effect explored here even if it limited the rupture speed (Figure 14 suggests that such deformation would be restricted to the SE rupture front). Investigating this will require running bimaterial models with off-fault damage, as was carried out by *Ben-Zion and Shi* [2005] but with slip-weakening friction.

4.6.4. Thermal Weakening

[70] It is generally agreed that at seismic slip speeds the most important mechanisms of fault weakening are thermal in origin [*Rice and Cocco*, 2007]. How these might interact with bimaterial effects is uncertain. For very small slip distances, up to several times the rate-and-state D_c, flash heating of local contact points may dominate. In this regime the macroscopic normal stress is thought to be unimportant, as the true contact area adjusts itself to maintain stresses that are a significant fraction of the elastic modulus. For greater slip distances, dependent upon the fault permeability but certainly larger than several times D_c, thermal pressurization of pore fluid is expected to dominate. To the extent that this might increase the pore pressure to values near σ_n^∞, it might be expected to diminish the relevance of a bimaterial reduction in σ_n. However, this pressurization is sensitive to the macroscopic rate of work on the fault $\tau v = |\sigma_n| f v$. Because the bimaterial effect we are describing operates at only modest reductions in σ_n ($\Delta\sigma_n/\sigma_n^\infty \approx \Delta f$) but increases the slip speed at the SE front to several times that at the NW front, thermal pressurization could augment the bimaterial effect, at least for the slips of order centimeters that are relevant for magnitude 1–3 earthquakes. *Ampuero and Ben-Zion* [2006] recently carried out simulations with strong velocity-weakening and found that for a wide range of parameters and heterogeneity the potency (area-weighted slip) was substantially stronger SE than NW of the nucleation site. They also observed the initiation of secondary slip pulses at the SE rupture front, much as in our slip-weakening simulations, suggesting that upon rupture arrest the stress field might retain qualities of the asymmetry discussed here, although a different role for the stopping phases is certainly implied.

4.7. Role of Regularization

[71] Currently, there is no generally agreed-upon scheme for regularizing bimaterial calculations. Our simulations shed some light on this issue. We find that for rapid evolution of the effective normal stress relative to slip-induced changes in friction ($\delta_\sigma/\delta_c \ll 1$), further reductions in δ_σ/δ_c cause the simulations to converge over greater and greater propagation distances. Because the laboratory basis for any assumed constitutive response to normal stress changes is exceedingly meager, this result is somewhat comforting. That is, provided the simulations are limited to the appropriate propagation distance, it suggests that the details of the adopted constitutive law are not of paramount importance. Simulations done without regularization (instantaneous response to normal stress changes, as in the work of, e.g., *Shi and Ben-Zion* [2006]) are consistent with the notion that the true response should be "fast" in some sense, but it seems preferable to ensure that the response is both fast and resolvable, to avoid the spurious oscillations in slip velocity that otherwise result. We have focused on the regime $\delta_\sigma/\delta_c \ll 1$ because this maximizes the

influence of the material mismatch and because we share the intuitive notion that the response to normal stress changes should be fast. Admittedly, the latter is a poor justification. On a superficial level this intuitive view is consistent with the experimental results of *Linker and Dieterich* [1992] but not *Prakash* [1998]. *Andrews and Harris* [2005] state that slip pulses are not important during rupture on bimaterial interfaces but base this conclusion on simulations in which $\delta_\sigma/\delta_c \sim 1$. Under these conditions the effective normal stress does not keep pace with the large normal stress changes in the slip-weakening zone, and the bimaterial effect is minimized (Figure 8).

[72] This is not to say that the details of the regularization are irrelevant when $\delta_\sigma/\delta_c \ll 1$. In Figure 7 we showed that for growing ruptures, slip pulses do not result when σ_n^* evolves with slip alone, although for pure time or combined slip and time evolution pulses form at velocities so close to the limiting speed that they may be geologically irrelevant. A more significant difference may occur in conjunction with the transition to supershear rupture speeds. For pure time evolution, as in Figure 13f, large stress drops lead to rupture velocities near C_{GR} at the positive front and C_{P_1} at the negative front. For pure slip evolution, on the other hand, over the same propagation distances and for otherwise identical conditions it is the negative front that propagates at C_{GR}, while the positive front spawns a slip pulse that propagates at supershear speeds (although less than C_{P_1}). At the negative (NW) front this is easily rationalized; for pure slip evolution $\Delta\sigma_n^*$ ahead of the rupture front is zero (because $\delta = 0$) so the tensile $\Delta\sigma_n$ there does not facilitate the transition to supershear velocities. At the positive (SE) front the supershear slip pulse does not arise until slip velocities are so large that $\Delta\sigma_n^*$ is no longer properly resolved; more dedicated simulations would be required to see if it survives more faithful adherence to the governing equations.

5. Conclusions

[73] We have run numerous models of slip-weakening ruptures on bimaterial interfaces to investigate the asymmetric distribution of aftershocks along the central San Andreas fault. For our relatively smooth and monotonically increasing driving stresses, the ruptures grow as bilateral cracks. For subshear ruptures, the normal stress change is compressive ahead of the SE-propagating front and tensile behind; the reverse is true at the NW front. When the NW front encounters a stress barrier, it slows and stops as it would in a homogeneous medium. In contrast, when the SE front encounters a barrier, for sufficiently large $\Delta\sigma_n$ the tensile stress pulse behind the SE front spawns a dying slip pulse that moves ahead of the slowing crack. If this slip pulse propagates farther than the crack, it smooths the stress field and reduces the stress concentration beyond the SE margin of the rupture. In addition, because the tensile stress that carried the slip pulse well into the barrier is transient, it leaves the SE margin, unlike that to the NW, far below the failure threshold. These mechanisms seem sufficient to explain the magnitude of the observed aftershock asymmetry, although the persistence of that asymmetry over moderately long timescales remains to be understood. A simple rate-and-state friction model suggests that the tensile stress pulse that continues down the fault to the SE is too short to immediately trigger slip and so is unlikely to contribute significantly to the aftershock asymmetry.

[74] Our simulations indicate that the slip pulse propagates farther than the crack provided the normal stress change $\Delta\sigma_n$ behind the SE front approaches or exceeds the nominal strength drop $\Delta\tau^{p-r}$. This result appears to be robust with respect to the assumed regularization of the normal stress response. A dimensional analysis based on Weertman's steady-state solution suggests that for a given contrast in shear wave speeds, the ratio $\Delta\sigma_n/\Delta\tau^{p-r}$ depends primarily upon the instantaneous rupture velocity. For a given stress drop $\tau^\infty - f_d|\sigma_n|$ this in turn implies a minimum propagation distance for this mechanism of asymmetry to become effective. Dimensional analysis and our numerical simulations also suggest that generating significant asymmetry while limiting the off-fault dynamic stresses requires large velocity contrasts that are nonetheless consistent with those inferred previously for this section of the San Andreas [*McGuire and Ben-Zion*, 2005].

[75] These simulations also shed light on the issue of bilateral versus unilateral rupture on bimaterial interfaces. As with the simulations of *Harris and Day* [1997], we find that slip-weakening friction under smooth loading conditions leads to slightly asymmetrical bilateral growth. This is in contrast to the predominantly unilateral ruptures produced by triggering stresses that are too short to permit significant slip-weakening, as in most of the cases studied by *Shi and Ben-Zion* [2006]. Although we continue to interpret the observed aftershock asymmetry as a manifestation of a material contrast across the fault, our simulations are consistent with this asymmetry resulting from ruptures that are essentially bilateral. Simulations with differing degrees of heterogeneity may be required to see if for some range of parameters the SE front is better able to "bust through" potential barriers and give rise to more unilateral ruptures. Our simulations and microearthquake observations are suggestive of additional asymmetry in the form of a greater tendency for subevents in compound earthquakes to be offset from the hypocenter in the negative direction. The simulations also suggest that long-term asymmetry in the level of damage on opposite sides of the fault, as observed by *Dor et al.* [2005, 2006], could result from predominantly bilateral rupture.

Appendix A: Steady-State Bimaterial Properties

[76] Weertman's equations for $\bar{\mu}$ and μ^* are corrected for a typographical error and simplified by *Cochard and Rice* [2000]. Defining $\bar{\mu}$ to be twice Weertman's value,

$$\mu^* = \frac{2\mu_1\mu_2}{\Delta}\left[\mu_1\left(\gamma_1\beta_1 - \alpha_1^4\right)\left(\gamma_2\beta_2 - \alpha_2^2\right) - \mu_2\left(\gamma_2\beta_2 - \alpha_2^4\right)\left(\gamma_1\beta_1 - \alpha_1^2\right)\right], \tag{A1}$$

$$\bar{\mu} = \frac{4\mu_1\mu_2}{\Delta}\left[\mu_1\gamma_2\left(1 - \alpha_2^2\right)\left(\gamma_1\beta_1 - \alpha_1^4\right) + \mu_2\gamma_1\left(1 - \alpha_1^2\right)\left(\gamma_2\beta_2 - \alpha_2^4\right)\right], \tag{A2}$$

where, with $i = 1$ or 2 and C being the steady-state rupture speed,

$$\alpha_i \equiv \sqrt{1 - C^2/2C_{S_i}^2}\ , \tag{A3}$$

$$\beta_i \equiv \sqrt{1 - C^2/C_{S_i}^2}\ , \tag{A4}$$

$$\gamma_i \equiv \sqrt{1 - C^2/C_{P_i}^2}\ , \tag{A5}$$

and

$$\begin{aligned}\Delta = {} & \mu_1^2(1-\gamma_2\beta_2)(\gamma_1\beta_1 - \alpha_1^4) + \mu_2^2(1-\gamma_1\beta_1)(\gamma_2\beta_2 - \alpha_2^4) \\ & + \mu_1\mu_2\left[(1-\alpha_1^2)(1-\alpha_2^2)(\gamma_1\beta_2 + \gamma_2\beta_1)\right. \\ & \left. + 2(\gamma_1\beta_1 - \alpha_1^2)(\gamma_2\beta_2 - \alpha_2^2)\right]\ .\end{aligned} \tag{A6}$$

[77] The generalized Rayleigh speed, if it exists, is the value of C at which the bracketed expression on the right side of (A2) equals zero. For $C = 0$ the values of μ^* and $\bar{\mu}$ become

$$\begin{aligned}\mu_0^* = {} & 2\mu_1\mu_2[\mu_2(1-2\nu_1) - \mu_1(1-2\nu_2)] \\ & \Big/\Big[4\{\mu_2(1-\nu_1) + \mu_1(1-\nu_2)\}^2 \\ & -\{\mu_2(1-2\nu_1) - \mu_1(1-2\nu_2)\}^2\Big],\end{aligned} \tag{A7}$$

$$\begin{aligned}\bar{\mu}_0 = {} & 8\mu_1\mu_2[\mu_2(1-\nu_1) + \mu_1(1-\nu_2)] \\ & \Big/\Big[4\{\mu_2(1-\nu_1) + \mu_1(1-\nu_2)\}^2 \\ & -\{\mu_2(1-2\nu_1) - \mu_1(1-2\nu_2)\}^2\Big],\end{aligned} \tag{A8}$$

where the subscript 0 denotes quasi-static deformations.

[78] For homogeneous media equations (A1) and (A2) become

$$\mu^* = 0\ , \tag{A9}$$

$$\bar{\mu} = 2\mu\frac{\beta\gamma - \alpha^4}{\beta(1-\alpha^2)}\ . \tag{A10}$$

[79] For $C = 0$ the latter becomes

$$\bar{\mu}_0 = \frac{\mu}{1-\nu}\ . \tag{A11}$$

[80] The right side of (A11) is simply the effective elastic modulus (here called μ') for quasi-static plane strain deformation. Furthermore, we can define the effective modulus of a bimaterial to equal μ' of a homogeneous medium having the same shear stress/shear displacement relation (that is, for a bimaterial $\mu' \equiv \bar{\mu}_0$).

[81] Inserting $\mu' = \bar{\mu}_0$ into (A10) and rearranging, for a homogeneous medium at nonzero rupture speeds we have

$$\frac{\bar{\mu}}{\mu'} = (1-\nu)\left[4\gamma - \left(1+\beta^{-2}\right)^2\right]\frac{C_s^2}{C^2}\ . \tag{A12}$$

[82] The right side of (A12) is identically the inverse of the function f_{II} introduced by *Rice* [1980, equation 5.35], as the scale factor relating static elastic crack and dislocation solutions to steady-state dynamic solutions. Thus the quantity $\mu'/\bar{\mu}$ (or $\bar{\mu}_0/\bar{\mu}$) generalizes Rice's expression for f_{II} to bimaterials.

Appendix B: Seismicity Rate Changes With Variable Normal Stress

[83] The evolution equation for the seismicity rate $R(t)$ due to an arbitrary load introduced by *Dieterich* [1994] [see also *Dieterich et al.*, 2000] can be summarized as:

$$R = \frac{r}{\gamma\dot{S}_r}\ , \tag{B1}$$

$$a\sigma\ \dot{\gamma} = 1 - \gamma\ \dot{S}\ , \tag{B2}$$

$$\dot{S} = \dot{\tau} - (f - \alpha)\ \dot{\sigma}\ , \tag{B3}$$

where γ is a state variable, S is a modified Coulomb stress function, r is the steady-state earthquake rate at the background stressing rate $\dot{S}_r$, a is the rate-and-state direct effect, and α affects the the response to normal stress changes. This equation has been often integrated under the assumption that changes in normal stress σ are small compared to the absolute σ. For instance, if $\dot{S}$ is smooth and a piecewise constant time-discretization of $S(t)$ is adopted, i.e., assuming $\dot{S}(t) = \dot{S}_n$ within a timestep $\Delta t_n = t_{n+1} - t_n$, it can be shown that:

$$\gamma_{n+1} = \frac{1}{\dot{S}_n} + \left(\gamma_n - \frac{1}{\dot{S}_n}\right)\exp\left[-\frac{\dot{S}_n}{a\sigma}\Delta t_n\right]\ . \tag{B4}$$

[84] If fluctuations of σ are large, we introduce the variables

$$\Gamma \doteq \sigma\gamma, \tag{B5}$$

$$\dot{S}' \doteq \frac{\dot{S} - a\dot{\sigma}}{\sigma}. \tag{B6}$$

[85] The evolution equation becomes:

$$a\ \dot{\Gamma} = 1 - \Gamma\ \dot{S}'\ . \tag{B7}$$

[86] For numerical integration, we assume piecewise constant $\dot{S}'(t)$ with the following approximation

$$\dot{S}'_n \approx \frac{\dot{\tau}_n - \left(f_{n+1/2} - \alpha + a\right)\dot{\sigma}_n}{\sigma_{n+1/2}} \tag{B8}$$

and get

$$\Gamma_{n+1} = \frac{1}{\dot{S}'_n} + \left(\Gamma_n - \frac{1}{\dot{S}'_n}\right)\exp\left[-\frac{\dot{S}'_n}{a}\Delta t_n\right]\ . \tag{B9}$$

[87] **Acknowledgments.** We thank Alain Cochard for providing us with a numerical code that could handle basically anything we threw at it. An MPI version (BIMAT) is now available through the Orfeus Seismological Software Library (http://www.orfeus-eu.org/links/softwarelib.htm). We also thank Alain Cochard, Ruth Harris, and Ares Rosakis for their helpful reviews. This work was supported by NSF under grant EAR-0126184. This is ETH contribution 1483.

References

Abercrombie, R. E. (1996), The magnitude-frequency distribution of earthquakes recorded with deep seismometers at Cajon Pass, southern California, *Tectonophysics*, *261*, 1–7.

Adams, G. G. (1998), Steady sliding of two elastic half-spaces with friction reduction due to interface stick-slip, *J. Appl. Mech.*, *65*, 470–475.

Ampuero, J.-P., and Y. Ben-Zion (2006), Macroscopic asymmetry of dynamic rupture on a bimaterial interface with velocity-weakening friction, *Eos Trans. AGU*, *87*(52), Fall Meet. Suppl., Abstract S53D-03.

Andrews, D. J. (1985), Dynamic plane-strain shear rupture with a slip-weakening friction law calculated by a boundary integral method, *Bull. Seismol. Soc. Am.*, *75*, 1–21.

Andrews, D. J. (2005), Rupture dynamics with energy loss outside the slip zone, *J. Geophys. Res.*, *110*, B01307, doi:10.1029/2004JB003191.

Andrews, D. J., and Y. Ben-Zion (1997), Wrinkle-like slip pulse on a fault between different materials, *J. Geophys. Res.*, *102*, 553–571.

Andrews, D. J., and R. A. Harris (2005), The wrinkle-like slip pulse is not important in earthquake dynamics, *Geophys. Res. Lett.*, *32*, L23303, doi:10.1029/2005GL023996.

Ben-Zion, Y. (2006), Comment on "Material contrast does not predict earthquake rupture propagation direction" by R. A. Harris and S. M. Day, *Geophys. Res. Lett.*, *33*, L13310, doi:10.1029/2005GL025652.

Ben-Zion, Y., and D. J. Andrews (1998), Properties and implications of dynamic rupture along a material interface, *Bull. Seismol. Soc. Am.*, *88*, 1085–1094.

Ben-Zion, Y., and Z. Shi (2005), Dynamic rupture on a material interface with spontaneous generation of plastic strain in the bulk, *Earth Planet. Sci. Lett.*, *236*, 486–496.

Breitenfeld, M. S., and P. H. Geubelle (1998), Numerical analysis of dynamic debonding under 2d in-plane and 3d loading, *Int. J. Fract.*, *93*, 13–38.

Chester, F. M., J. P. Evans, and R. L. Biegel (1993), Internal structure and weakening mechanisms of the San Andreas fault, *J. Geophys. Res.*, *98*, 771–786.

Cochard, A., and J. Rice (2000), Fault rupture between dissimilar materials: Ill-posedness, regularization, and slip-pulse response, *J. Geophys. Res.*, *105*, 25,891–25,907.

Crouch, S. L., and A. M. Starfield (1983), *Boundary Element Methods in Solid Mechanics*, Allen and Unwin, St Leonards, NSW, Australia.

Dieterich, J. H. (1994), A constitutive law for rate of earthquake production and and its application to earthquake clustering, *J. Geophys. Res.*, *99*, 2601–2618.

Dieterich, J. H., V. Cayol, and P. Okubo (2000), The use of earthquake rate changes as a stress meter at Kilauea volcano, *Nature*, *408*, 457–460.

Dor, O., C. Yildrim, T. K. Rockwell, O. Emre, Y. Ben-Zion, M. Sisk, and T. Duman (2005), Asymmetric structural properties across the 1943 rupture zone of the North Anatolian fault: A possible indication for a preferred rupture direction, *Eos Trans. AGU*, *86*(52), Fall Meet. Suppl., Abstract S31B-07.

Dor, O., T. K. Rockwell, and Y. Ben-Zion (2006), Geological observations of damage asymmetry in the structure of the San Jacinto, San Andreas and Punchbowl faults in southern California: A possible indicator for preferred rupture propagation direction, *Pure Appl. Geophys.*, *163*, 301–349.

Eberhart-Phillips, D., and A. J. Michael (1998), Seismotectonics of the Loma Prieta, California region and determined from three-dimensional v_p, v_p/v_s, and seismicity, *J. Geophys. Res.*, *103*, 21,099–21,120.

Freund, L. B. (1990), *Dynamic Fracture Mechanics*, Cambridge Univ. Press, New York.

Harris, R. A., and S. M. Day (1997), Effects of a low–velocity zone on a dynamic rupture, *Bull. Seismol. Soc. Am.*, *87*, 1267–1280.

Harris, R. A., and S. M. Day (2005), Material contrast does not predict earthquake rupture propagation direction, *Geophys. Res. Lett.*, *32*, L23301, doi:10.1029/2005GL023941.

Harris, R. A., and S. M. Day (2006), Reply to comment on "Material contrast does not predict earthquake rupture propagation direction", *Geophys. Res. Lett.*, *33*, L13311, doi:10.1029/2006GL026811.

Linker, M. F., and J. H. Dieterich (1992), Effects of variable normal stress on rock friction: Observations and constitutive equations, *J. Geophys. Res.*, *97*, 4923–4940.

McGuire, J. J., and Y. Ben–Zion (2005), High–resolution imaging of the Bear Valley section of the San Andreas fault at seismogenic depths with fault–zone head waves and relocated seismicity, *Geophys. J. Int.*, *163*, 152–164, doi:10.1111/j.1365–246X.2005.02703.x.

Oglesby, D. D., and S. M. Day (2002), Stochastic fault stress: Implications for fault dynamics and ground motion, *Bull. Seismol. Soc. Am.*, *92*, 3006–3021.

Pollard, D. D., and P. Segall (1987), Theoretical displacements and stresses near fractures in rock: With applications to faults, joints, veins, dikes, and solution surfaces, in *Fracture Mechanics of Rock*, edited by B. K. Atkinson, pp. 277–349, Elsevier, New York.

Prakash, V. (1998), Frictional response of sliding interfaces subjected to time–varying normal pressures, *J. Tribol.*, *120*, 97–102.

Ranjith, K., and J. R. Rice (2001), Slip dynamics at an interface between dissimilar materials, *J. Mech. Phys. Sol.*, *49*, 341–361.

Rice, J. R. (1980), The mechanics of earthquake rupture, in *Physics of the Earth's Interior*, edited by A. M. Dziewonski and E. Boschi, *Proc. Int. Sch. Phys. Enrico Fermi*, *78*, 555–649.

Rice, J. R., and M. Cocco (2007), Seismic fault rheology and earthquake dynamics, in *Tectonic Faults: Agents of Change on a Dynamic Earth*, edited by M. R. Handy et al., pp. 99–138, MIT Press, Cambridge, Mass.

Rice, J. R., and A. L. Ruina (1983), Stability of steady frictional slipping, *J. Appl. Mech.*, *50*, 343–349.

Rice, J. R., N. Lapusta, and K. Ranjith (2001), Rate– and state–dependent friction friction and the stability of sliding between elastically deformable solids, *J. Mech. Phys. Sol.*, *49*, 1865–1898.

Rubin, A. M. (2002a), Aftershocks of microearthquakes as probes of the mechanics of rupture, *J. Geophys. Res.*, *107*(B7), 2142, doi:10.1029/2001JB000496.

Rubin, A. M. (2002b), Using repeating earthquakes to correct high–precision earthquake catalogs for time–dependent station delays, *Bull. Seismol. Soc. Am.*, *92*, 1647–1659.

Rubin, A. M., and J.-P. Ampuero (2005), Earthquake nucleation on (aging) rate and state faults, *J. Geophys. Res.*, *110*, B11312, doi:10.1029/2005JB003686.

Rubin, A. M., and D. Gillard (2000), Aftershock asymmetry/rupture directivity among central San Andreas fault microearthquakes, *J. Geophys. Res.*, *105*, 19,095–19,109.

Scholte, J. G. J. (1947), The range of existence of Rayleigh and Stonely waves, *Mon. Not. R. Astron. Soc., Geophys. Suppl.*, *5*, 120–126.

Shi, Z., and Y. Ben–Zion (2006), Dynamic rupture on a bimaterial interface governed by slip–weakening friction, *J. Geophys. Int.*, *165*, 469–484.

Uenishi, K., and J. R. Rice (2003), Universal nucleation length for slip–weakening rupture instability under nonuniform fault loading, *J. Geophys. Res.*, *108*(B1), 2042, doi:10.1029/2001JB001681.

Weertman, J. (1980), Unstable slippage across a fault that separates elastic media of different elastic constants, *J. Geophys. Res.*, *85*, 1455–1461.

Xia, K., A. J. Rosakis, H. Kanamori, and J. R. Rice (2005), Laboratory earthquake along inhomogeneous faults: Directionality and supershear, *Science*, *308*, 681–684.

J.-P. Ampuero, Institute of Geophysics, Swiss Federal Institute of Technology (ETH), CH–8093, Zurich, Switzerland.

A. M. Rubin, Department of Geosciences, Princeton University, Princeton, NJ 08544, USA. (arubin@princeton.edu)